UNIVERSITY OF PADOVA
Department of Industrial Engineering
Doctoral Program in Industrial Engineering
Curriculum: Electrical Engineering
Cohort XXXVI

DIGITAL IMPLEMENTATION OF INNOVATIVE ELECTRIC DRIVES

Thesis for the degree of Doctor of Philosophy

Prof. Giulio Rosati, Course Coordinator
Prof. Luigi Alberti, Candidate's Supervisor
Prof. Ludovico Ortombina, Candidate's Co-supervisor

Ph.D. Candidate: GIUSEPPE GALATI

Padua
November 29, 2023

You do not need to see the entire staircase.
Simply start by climbing the first step.

— Martin Luther King

ABSTRACT

Nowadays high efficient electric drives are needed to achieve maximum performance of an electric motor. Performance indeed, are a key factor in the industry world. Automotive sector for instance, is undergoing a radical shift from combustion engines to electric motors. Aircraft and navy, are moving towards the electrification of all the auxiliary services. In this scenario not only the performance are fundamental but even the capacity of the motor to withstand failure, i.e., fault-tolerant capability. The former one can be maximized by implementing an accurate motor control. A correct rotor position in this case is fundamental. Sensors such as encoder or resolver are used to obtain the rotor position information, i.e., sensored control. In the last years, many algorithms have been developed and investigated to eliminate the position sensor which has some drawbacks. First of all the overall price is increased because additional hardware and cabling are needed. More importantly, the reliability of the drive is decreased since position sensor fault is common. In a sensorless drive, no position sensor is needed because the rotor position is estimated by processing stator currents or voltages according to the motor speed range. Sensorless control allows reducing the overall price, motor frame size and more importantly increasing the reliability of the drive. Fault-tolerant capability, together with reliability of the drive and the need to achieve high power density, is increasing the attention on multiphase machines.

This dissertation aims at investigating sensorless control at standstill and low speed by using high frequency injection techniques. Motor anisotropy is depicted by analyzing the current response due to the high frequency injection. Since the motor parameters are different, several responses are obtained from different motors. As a consequence, the performance achievable in sensorless control are different for each machine. The ability of the motor to be controlled in sensorless control is defined as self-sensing capability.

The thesis can be divided into two main parts. In the first part, sensorless control applied to a multiphase machine with six phases is investigated. The machine is analyzed as two three-phase windings, each one supplied by a dedicated inverter. A fault-tolerant strategy is developed by studying the motor self-selfing capability. The novelty of the proposed research is that the self-sensing capability of the motor is enhanced and sensorless control without divergence is obtained. No complex compensation algorithms are applied. Finally, an application of the Kalman fusion algorithm to the sensorless control of aforementioned multiphase machine is investigated. Sensor fusion is adopted to combine together more estimated positions from more winding sets. The purpose is to close all three-phase windings control loops on one fused position. By doing so, fault-tolerant of the machine is enhanced in the case of a fault in the position sensor.

The second part of the thesis is focused on development of a novel observer transfer function for the rotating voltage signal injection. The novelty is that the whole estimator transfer function is retrieved in the Laplace domain by exploiting the modulation/demodulation theory. With this approach, the demodulation effects on filters transfer functions are considered and a proper observer transfer function is retrieved. As a consequence the observer regulator tuning allows achieving both maximum performance and the desired closed loop bandwidth.

The whole thesis was fully validated through an intensive simulation and experimental stage, except the rotating voltage injection which was tested only by simulation. The aforementioned contents were presented by the author at several international conferences and IEEE Journal papers. The complete list of publications is reported at end of the dissertation.

SOMMARIO

In questi ultimi tempi azionamenti elettrici sempre più efficienti sono necessari per raggiungere le massime performance di un motore elettrico. Inoltre, la resilienza ai guasti sta riscuotendo molto attenzione sia da parte del mondo della ricerca sia da quello dell'industria. Il settore automotive, ad esempio è interessato da un cambio radicale del sistema di trazione che sta passando dall'uso di motori a combustione a quelli elettrici. Anche altri settori come quello aereonautico o delle navi, si stanno muovendo verso un'elettrificazione maggiore, ad esempio rendendo sempre più elettrici tutti i sistemi ausiliari. Un controllo accurato di un motore elettrico ha bisogno della conoscenza della posizione del rotore per raggiungere le massime performance dell'azionamento elettrico. Di solito la posizione viene misurata attraverso l'uso di sensori come encoder o resolver denominando il controllo sensored del motore. Negli ultimi anni, sono stati sviluppati ed investigati diversi algoritmi per eliminare l'uso del sensore di posizione che ha qualche svantaggio. Prima di tutto il prezzo dell'intero azionamento elettrico è maggiore a causa del maggior hardware. Inoltre, cosa ancora più importante, l'affidabilità dell'azionamento diminuisce dato che un guasto nel sensore di posizione è molto comune. In un azionamento sensorless, il sensore di posizione viene eliminato perchè la posizione del rotore viene stimata analizzando ed elaborando correnti o tensioni di statore, in base al range di velocità dove sta lavorando il motore. Il controllo sensorless permette di ridurre il costo dell'azionamento, le sue dimensioni ed ancora più importante di aumentare l'affidabilità. Quest'ultima, insieme alla loro capacità di resilienza al guasto ed alla alta densità di potenza sta portando molta attenzione anche all'uso di motori elettrici multifase.

Il lavoro di tesi si propone l'obiettivo di sviluppare algoritmi di controllo sensorless a nulla o bassa velocità del motore attraverso l'iniziezione di segnali ad alta frequenza. La posizione del rotore viene stimata analizzando la risposta in alta frequenza del motore. Dato che i parametri del motore sono diversi, ogni motore ha una risposta dovuta all'iniezione in alta frequenza diversa. Di conseguenza, le performance raggiungibili dal controllo sensorless sono differenti per ogni macchina. L'abilità del motore di essere controllato senza sensore di posizione viene definita come self-sensing capability.

La tesi può essere divisa in due parti principali. Nella prima parte, viene sviluppato un algoritmo di controllo sensorless applicato ad un motore con sei fasi. La macchina viene analizzata come due avvolgimenti trifase distinti, ciascuno collegato ad un inverter dedicato. Studiando la self-sensing capability del motore, viene sviluppata una strategia di resilienza al guasto. L'aspetto innovativo della ricerca proposta è che la self-sensing capability del motore è migliorata. inoltre il controllo sensorless viene ottenuto senza nessuna divergenza e non vengono usate complesse tecniche di compensazione. Nella

parte finale, si analizza e si realizza un'applicazione dell'algoritmo di Kalman fusion al controllo sensorless. Lo scopo dell'applicazione è quello di unire propriamente le due posizioni stimate dai due avvolgimenti trifase in maniera tale da chiudere tutti e due gli anelli di controllo su un'unica posizione. In questa maniera, la capacità di resilienza al guasto della macchina è migliorata nel caso di un guasto del sensore di posizione.

La seconda parte si concentra sullo studio e la realizzazione di una nuova funzione di trasferimento dell'osservatore per l'iniezione rotante. La novità della ricerca sta nel fatto che la completa funzione di trasferimento viene trovata nel dominio di Laplace applicando la teoria della modulazione/demodulazione. In questo modo, gli effetti della demodulazione sulle funzioni di trasferimento dei filtri vengono considerate ed una propria funzione di trasferimento viene trovata. Di conseguenza, il tuning del regolatore permette di raggiungere la banda di controllo ad anello chiuso desiderata e le performance dell'azionamento vengono migliorate.

Il lavoro di tesi è stato completamento validato attraverso molteplici prove sperimentali, tranne che per il lavoro sull'iniezione rotante dove la nuova funzione di trasferimento è stata testata solo in simulazione. I contenuti appena citati sono stati esposti dall'autore in molteplici conferenze internazionali e riviste IEEE. La lista completa delle pubblicazioni è riportata nella parte finale della tesi.

CONTENTS

LIST OF FIGURES

LIST OF TABLES

ACRONYMS

IM	Induction Motor
AC	Alternating Current
PMSM	Permanent Magnet Synchronous Motor
SynR	Synchronous Reluctance
VSD	Vector Space Decomposition
n	Number of phases
MS	Multi Stator
l	Three-phase sets
BEMF	Back Electromotive Force
HF	High Frequency
IPM	Interior Permanent Magnet
DT	Dual Three-Phase Motor
KF	Kalman Filter
TF	Transfer Function
FEA	Finite Element Analysis
HPF	High Pass Filter
LPF	Low Pass Filter
PI	Proportional Integrator
REG	Regulator
RLS	Recursive Least Square
Q − PLL	Quadrature-PLL
HC	Half-Control
PE	Position Estimator
CTRL	Control
EF	Ellipse Fitting
MUT	Motor Under Test
REF	Reference Trajectory
COP	Constant Operating Points
CL	Closed Loop
OL	Open Loop
DS	Direct Synthesis
IMP	Internal Model Principle

NOMENCLATURE

$\alpha\beta$	Stationary reference frame
dq	Synchronous reference frame
$d^x q^x$	Estimated synchronous reference frame
R_s	Stator resistance
p	Pole pairs
λ_{mg}	Permanent magnet flux
u_α	α-axis stator voltage
u_β	β-axis stator voltage
i_α	α-axis stator current
i_β	β-axis stator current
λ_α	α-axis flux linkage
λ_β	β-axis flux linkage
L_α	α-axis apparent inductance
L_β	β-axis apparent inductance
l_α	Differential α-axis inductance
l_β	Differential β-axis differential
$l_{\alpha\beta}$	Differential $\alpha\beta$-axis inductance
$i_{h\alpha}$	α-axis high frequency current
u_d	d-axis stator voltage
u_q	q-axis stator voltage
i_d	d-axis stator current
i_q	q-axis stator current
i_d^m	Measured d-axis current
i_q^m	Measured q-axis current
i_d^{abc}	abc winding d-axis current
i_q^{abc}	abc winding q-axis current
i_d^{xyz}	xyz winding d-axis current
i_q^{xyz}	xyz winding q-axis current
i_d^k	Kalman d-axis current
i_q^k	Kalman q-axis current
l_{dd}	Differential d-axis inductance
l_{qq}	Differential q-axis inductance
l_{dq}	Differential cross inductance
l_Δ	Differential semi difference inductance
l_Σ	Differential mean value inductance
λ_d	d-axis stator flux linkage
λ_q	q-axis stator flux linkage
λ_d^{abc}	abc winding d-axis flux
λ_q^{abc}	abc winding q-axis flux
i_d^x	d^x-axis stator current

i_q^x	q^x-axis stator current
ω_m	Rotor mechanical speed
ω_{me}	Rotor electrical speed
ϑ_{me}	Measured electrical rotor position
U_h	Magnitude of the injected signal
ω_h	Pulsation frequency of the injected signal
$i_{h\beta}$	β-axis high frequency current
$\widehat{\vartheta}_{me}$	Estimated electrical rotor position
$\widehat{\vartheta}_{me}^{abc}$	abc winding estimated electrical position
$\widehat{\vartheta}_{me}^{xyz}$	xyz winding estimated electrical position
$\widehat{\vartheta}_{me}^{mean}$	Non-weighted average fused electrical position
$\widehat{\vartheta}_{me}^{k}$	Kalman fusion electrical position
$\widehat{\omega}_m$	Estimated mechanical speed
$\widehat{\omega}_{me}$	Estimated electrical speed
$\widetilde{\omega}_{me}$	Electrical speed error
ϵ	Open loop estimation error
ϵ'	Error signal
$\Delta\vartheta_{me}$	Position error
$\Delta\vartheta_{me}^{abc}$	abc set position error
$\Delta\vartheta_{me}^{xyz}$	xyz set position error
$\Delta\vartheta_{me}^{mean}$	Non-weighted average position error
$\Delta\vartheta_{me}^{k}$	Kalman fusion position error
t_1	Sensored trajectory
t_2	Sensorless trajectory
t_1^m	Measured sensored trajectory
t_2^m	Measured sensorless trajectory
t_1^f	Estimated sensored trajectory
t_2^f	Estimated sensorless trajectory
ξ_{pll}	Q-PLL damping factor
K_p	Proportional gain
K_i	Integral gain
ω_{pll}	Q-PLL natural pulsation
ω_{obs}	Observer bandwidth
ω_x	Generic pulsation frequency
ξ_{obs}	Observer damping factor
$\mathbf{w}$	Process noise vector
$\mathbf{v}$	Measurement noise vector
$\mathbf{y}$	Output vector
$\mathbf{C}$	Observation matrix
$\mathbf{Q}$	Process noise covariance matrix
$\mathbf{R}$	Measurement noise covariance matrix
$\mathbf{I}$	Identity matrix
$F_{\mathrm{HPF}}(s)$	High pass filter transfer function

$F_{\mathrm{LPF}}(s)$	Low pass filter rransfer function
$F_{\mathrm{HPF}}^{\Sigma}(s)$	New high pass filter transfer function
$G_d(s)$	d-axis motor dynamic
$G_q(s)$	q-axis motor dynamic
$\zeta(t)$	Generic demodulated signal in time
ϕ	Arbitrary phase shift
$x(t)$	Generic signal in time
$\mathcal{L}$	Laplace operator
$\mathrm{R(s)}$	Regulator transfer function
$\mathrm{P(s)}$	Plant transfer function
$\mathrm{F(s)}$	Feedback transfer function
$\mathrm{W^*(s)}$	Desired closed loop transfer function
$P_{\mathrm{obs}}^{\mathrm{new}}(\mathrm{s})$	Proposed observer transfer function
$P_{\mathrm{obs}}^{\mathrm{old}}(\mathrm{s})$	Conventional observer transfer function

1 Introduction

High efficiency electric drives and maximum performance of the motors are key targets in nowadays projects. First electric drives were made using Induction Motor (IM) thanks to their low production cost. The increasing energy costs and the new environmental challenges are driving the electric drives sector to use different Alternating Current (AC) motors such as the Permanent Magnet Synchronous Motor (PMSM) [1]. Synchronous machines are gaining increasing interest thanks to their fast dynamic response, good overload capability and high energy density. Among the synchronous machines, due to the high cost of the permanent magnet and the pollution created during the mining operation, different solutions have been investigated. A viable alternative can be identified in the Synchronous Reluctance (SynR) motors. The robustness, the wide operating range and the absence of permanent magnets made these motors more and more attractive over the years. Moreover, due to the electrification process of energy production, transportation [2] and thanks to the significant cost reduction of the power electronics components, multiphase machines [3] have attracted great attention. The increase of the number of phases allow the reduction of the phase current, hence high dynamics can be reached for high power systems usually characterized by low dynamic and high current. Multiphase machines can be studied with different approaches developed in the literature.

Multiple orthogonal subspaces using a dedicated matrix are the result of the Vector Space Decomposition (VSD). Energy conversion and torque production are performed in the machine's time-fundamental model, i.e., a single subspace. The other subspaces map the harmonic patterns of the machine [4–6]. A great advantage of the VSD is that can be applied to machines either with a symmetrical or asymmetrical windings configuration. Defining the Number of phases (n), the spatial shift between two consecutive windings is $2\pi/n$ for the symmetrical configuration whereas a machine is asymmetrical if the phase shift between the corresponding phases of the winding sets is π/n. All the control algorithms defined for a three-phase machine can be applied with the VSD method, i.e., VSD-based pulse width modulation techniques, space vectors and carrier based methods [7–10]. Moreover, most fault-tolerant strategies for multiphase machines based on open phase fault are based on the control of the harmonic subspaces [11, 12]. Nevertheless, VSD approach has limitation in the modelling of the modular configuration of the stator windings for a multiphase machine, namely, when the stator is made up of more three-phase windings. Indeed, only the total torque of the machine is retrieved with the VSD approach, whereas is impossible to determine the torque production of each three-phase winding set. Furthermore, the pulse width modulation techniques applied for the VSD increment their complexity

with the number of phases. Usually, in case of open circuit fault, the entire redefinition of the modulation technique needs to be done [13].

Multi Stator (MS) approach is the second modelling method used for multiphase machines [14]. A modular configuration of the stator windings can be described by modelling the machine as multiple winding sets operating in parallel. Thus, solving the drawback of the VSD in describing modular configurations. Each set must consists of l three-phase winding sets ($l \geq 1$), with an isolated neutral point treated with a dedicated VSD transformation [15]. Power converters can be designed as multiple three-phase modules with great advantages in terms of size and costs. Multi three-phase machines are widely described with the MS approach. The stator is split in several three-phase windings and each set is described through its own time-fundamental VSD subspace. Therefore, for a machine with l winding sets, l time-fundamental VSD subspaces are obtained [16, 17]. Torque production is possible to be exhibited for each different subspace. MS method can be described as a modular application of the VSD approach to multiphase machines. The modularity allow implementing independent modular modulation algorithms. The major drawback of the MS approach is the magnetic coupling between each winding sets [18]. Instability issues of the control algorithm can arise. A decoupling method for the MS approach is described in [19].

Describing correctly the machine is not enough to develop an effective motor control. Indeed, an accurate knowledge of the rotor position is mandatory to reach optimal performance of a PMSM. Encoder or resolver are used to obtain the rotor position defining the sensored control. The use of this kind of sensors increase the overall price and decrease the reliability of the drive. Additional hardware and cabling are the main drawbacks. Several position estimation algorithms have been developed to remove the position sensor by reducing the motor frame size, lowering the price and increasing the reliability of the drive. In a sensorless drive, the estimated position is used for motor control and no position sensor is needed. Sensorless algorithms can be bundled into two groups according to the operating speed of the motor.

At medium-high speed range, the rotor position is estimated through a reconstruction of the Back Electromotive Force (BEMF) [20, 21] or the active flux [22, 23]. These variables are calculated through the measurement of currents and stator voltages, which amplitude is proportional to the rotor speed. As a consequence these methods can be applied only in medium and high speed range.

At standstill and low speed region, rotor anisotropy is exploited through additional High Frequency (HF) injection in the stator windings. Several algorithms have been investigated and can be bundled into two groups, according to the reference frame in which the methods are applied or the type of injected signal. In the former, an HF signal is superimposed to the fundamental voltage reference in the estimated synchronous reference frame, usually the

d-axis [24,25]. The rotor position is retrieved by the minimization of the measured pulsating current along the estimated q-axis with the use of an observer. In the latter group, the HF voltage signals are superimposed to the fundamental voltage references in the stator reference frame [26,27], called rotating signal injection sensorless techniques. These algorithms estimate the rotor position by demodulating the negative sequence carrier current through a synchronous reference frame filter and an observer. It is worth noting that Interior Permanent Magnet (IPM) and SynR motors are more suitable to HF thanks to their pronounced anisotropy.

HF injection depicts the rotor anisotropy by analyzing the current response. Several responses are obtained by each motor since the parameters are different, hence the performance achievable in sensorless control can be different for each machine. Moreover, the operating point of the machine changes the frequency response since magnetic saturation and cross coupling occur at high current. The former reduces the rotor anisotropy, reducing the signal-to-noise ratio of the position estimation. The latter one introduces a position estimation error which degrades the electric drive performance and it could lead to stability issues. To eliminate or reduce the position error, several complex compensation methods have been developed for three-phase motors [28–30]. Low speed sensorless algorithms and compensation techniques have been applied even to multiphase machines in [31–35]. In [32], a six-phase motor is used. MS approach is used to describe the machine as two three-phase sets, namely, Dual Three-Phase Motor (DT). A new degree of freedom is provided by the additional three-phase winding. The method takes advantage of the additional degree of freedom of DT motor reducing both the torque and the dc-link current ripple. The method is applied to a PMSM and a constant steady-state error is shown. A different approach is used in [33] where the high frequency signals are injected in only one three-phase electrical winding. The method is applied on a low voltage PMSM and good performance is achieved. The zero sequence voltage is exploited in [34] to estimate the rotor position and the undesired harmonic is suppressed by applying an optimal phase shift between the two independent injected signals. However, a quite large constant estimation error is reported. A compensation method based on current pulse injection is investigated in [35]. The additional degree of freedom of a DT PMSM is exploited to estimate motor parameters and, in turn, improve the sensorless accuracy.

Sensorless control on multiphase machine can be also applied by implementing sensor fusion techniques. Thanks to the modularity provided by the MS approach, a machine with l three-phase sets can be supplied by l inverter. Moreover, a position estimation algorithm can be applied for each winding sets resulting in l estimated positions. Sensor fusion algorithms can be used to merge the l estimated positions into an unique fused estimated variable. Hence, sensorless control can be performed. Kalman Filter (KF) [36,37] is

one of the most significant. In [38, 39], multi-sensor data fusion techniques based on KF are applied to electric motors. Two different approaches to KF for sensor fusion are reported in the literature. The former one is called measurement fusion and it simply merges the multi-sensor data incrementing the size of the observation vector [40, 41]. The latter is called state fusion and it consists on multiple KF that run in parallel on different models. The outputs of the bank of KF are then merged together using the minimum mean square error estimation to obtain an unique weighted measurement as final estimation [42, 43]. The main difference between the two approaches is the computational load. Incrementing the size of the observation vector results in an higher computational cost. Nevertheless, if the sensors' matrices have different sizes, the second approach may be inapplicable.

To conclude, the performance of an electric drive are influenced even by how the whole plant model is described. In an electric drives, several control loops interacts with each other, hence an accurate plant model must be provided to use model-based design methods. Which are the main algorithms developed in this dissertation. A sensorless plant scheme contains the current and speed loops that interact with each other and with the observer regulator [44]. Therefore, an inaccurate description of the observer Transfer Function (TF) could lead to instability issues and inaccuracy of the estimated position. Both time and Laplace domain variables are reported in a sensorless system representation. However, the conventional approach usually derive the observer TF in time domain by adding filter TFs only a posteriori leading to an incorrect design of the observer regulator. In [45] a new observer TF is proposed by exploiting the modulation/demodulation theory in the Laplace-domain for the pulsating signal injection. Regarding the rotating signal injection the literature still reports an observer TF representation obtained by blending together both time and Laplace-domain expressions [46]. Therefore, an accurate tuning of the controller and accuracy of the position estimation cannot be performed.

This dissertation wants to give its contribution into low speed sensorless control for three-phase and multiphase motors, hoping to provide interesting insights into future research. In Section 1.1, the critical aspects and the main contribution of the dissertation are summarized.

1.1 Investigated Aspects and Contribution

Within the scenario outlined above, the thesis investigates the design and implementation of sensorless control algorithms in the low speed or standstill speed range. Both three-phase and multiphase electric motors are considered. The challenges on which the thesis is focused on and the proposed solutions are summarised in the following subsections.

1.1.1 Self-Sensing Capability Investigation

Challenge. Sensorless control relies on the motor parameters to reach maximum accuracy of the estimated position. Since the motor parameters are different for each machine, several responses to the high frequency injection can be obtained. As a consequence, since the response of the machine is analyzed to retrieve the rotor position in the standstill and low speed range, the accuracy of the latter is affected. Moreover, due to the cross inductances, an estimation error appears. As a consequence, the estimated position is not the same as the actual one, especially when the machine is operating at high current, i.e., is saturated. Different responses are obtained for different machines, hence if the estimation error is too big, sensorless control divergence can occur. As aforementioned, the operating point on which sensorless control divergence can appear is different for each machine.

In the outlined scenario is important to characterize the ability of the motor to be controlled in sensorless mode, i.e., the self-sensing capability of the machine.

Contribution. A sensorless control strategy that allow enhancing the fault-tolerant capability of a six-phase motor is retrieved. The strategy is developed by studying the motor self-sensing capability. The motor is decomposed in two three-phase sets using the MS approach and each set is supplied by a dedicated inverter. The developed strategy uses the new degree of freedom given by the second set to control the motor without position sensor with an almost zero estimation error. The method is based on the verified assumption that cross inductance terms responsible for the estimation error are negligible when the motor is low saturated, i.e., at low current. Hence, a set is used at low operating points to estimate the correct rotor position. Therefore, both three-phase sets are closed on the estimated position from the set operating at low current. The developed control strategy allow controlling the second set up to its nominal current and overloaded without sensorless control divergence. Moreover, the estimated position is accurate and not affected by the estimation error due to cross-magnetic saturation that is the main flaw of low speed algorithm and no motor parameters are required.

The developed sensorless control strategy reduces the available torque at motor shaft since a three-phase set has to operate at low current to estimate the correct rotor position. However, the main application for which the strategy was developed is a fault in the position sensor. In this case, the fault-tolerant capability of the motor is enhanced by applying sensorless control without using complex compensation methods. The control strategy it is not changed, indeed is enough to reduce the current in one set and estimate with it the rotor position to close both control loops. The study is validated both through Finite Element Analysis (FEA) of the adopted motor and an extensive experimental stage.

1.1.2 Sensor Fusion Algorithm

Challenge. This study takes into consideration the sensorless control strategy developed in Section 1.1.1, as well as the same machine. It is worth remembering that the presented sensorless control strategy uses the two sets at different operating points. Only the estimated position from the winding that operates at low current is used in the study briefly described in Section 1.1.1. However it is possible to estimate the rotor position even with the second three-phase set. In this case, two estimated positions are available in the control and since the estimation error is different depending of the operating point of the machine, one position may be more truthful than the other one.

The main challenge faced by this study is how to combine the two estimated position in a proper way to obtain an unique estimated rotor position to close both control loops.

Contribution. The main idea of the study is to merge together with an appropriate algorithm the two estimated positions, i.e., input variables. The unique merged variable is used to perform sensorless control.

Two fusion techniques are adopted and compared, a mean average and an application of Kalman filter sensor fusion. In the former approach, same weight is assigned to both estimated position whereas different weight is assigned with the latter one. Kalman filter sensor fusion fuses together the estimated position of the two three-phase sets. The unique obtained state is the result of a proper weight of the two input variables. As aforementioned, the weight of an estimated position is a function of the operating point of the winding set. The weight to assign at each estimated position is found experimentally by an extensive experimental stage to validate both different supply scenario and the developed study. Sensorless control is performed without using compensation methods and the estimation error is almost nullified. The investigation is conducted taking a fault in the position sensor as a reference scenario.

1.1.3 Modelling of a Position Observer

Challenge. An observer is used to retrieve the rotor position in a low speed sensorless electric drive. The regulator inside the observer has to interact with speed and current loops. To tune the regulator and reach optimal performance of the electric drive, model based design methods are mostly used. As a consequence, when using this approaches, an accurate plant model is mandatory.

The main challenge that this study faces is that rotating signal injection observer TF is retrieved by mixing together time and Laplace domain variables. As aforementioned this leads to not considering demodulation effects on filters TFs. Hence, the sensorless plant is not well described and this could lead to instability issues of the electric drive. Furthermore, the design performance

of the observer can not be reached.
Contribution. The whole rotating voltage injection TF is retrieved in the Laplace domain. Modulation/demodulation effects on filters TFs are considered and an optimal description of the plant is obtained. The plant TF is retrieved by exploiting the modulation/demodulation theory. Simulation results validate the developed position observer by analyzing both the observer time response and the position tracking. Different regulators are designed by using both the Direct Synthesis (DS) and the Internal Model Principle (IMP) approaches to highlight the correctness of the proposed observer TF for the rotating injection based sensorless control.

1.2 Dissertation Outline

The dissertation consists of six chapters. The current chapter, Chapter 1, introduces the considered research topics, highlighting the main aspects on which the research activity reported herein is focused. The theoretical background about sensorless control and the different estimation algorithms used at low speed or standstill are described in Chapter 2. The studies carried out in the dissertation can be divided in two main groups. The first one is composed by two works regarding the sensorless control applied to a multiphase machine. In Chapters 3, 4 fault tolerant sensorless control strategies are performed using a dual three-phase synchronous reluctance motor in the case of a fault in the position sensor. In particular, Chapter 3 allow controlling the motor by using only one estimated position whereas a sensor fusion algorithm is implemented in Chapter 4 and both estimated positions are used in the control. The second part regards a new position observer retrieved completely in the Laplace domain for the rotating voltage signal injection and it is reported in Chapter 5 Finally, the general conclusions from the whole research work are reported in Chapter 6.

2 Sensorless Control at Low Speed or Standstill: Theoretical Background

In the following, the theoretical background of different HF injection sensorless techniques at low speed or standstill is described. Then, an exhaustive discussion about the estimation error introduced by sensorless control and how to compute and predict the ability of the motor to be controlled without position sensor is given.

2.1 Pulsating Signal-Injection

Pulsating signal-injection [47] is based on superimposition of HF voltage signals on the fundamental one in the synchronous dq reference frame. By omitting the time dependency of the stator variables to ease the notation, the stator voltage balance equations of a PMSM in the dq reference frame are:

$$\begin{aligned} u_d &= R_s i_d + \frac{d\lambda_d(i_d, i_q)}{dt} - \omega_{me}\lambda_q(i_d, i_q) \\ u_q &= R_s i_q + \frac{d\lambda_q(i_d, i_q)}{dt} + \omega_{me}\lambda_d(i_d, i_q) \end{aligned} \tag{2.1}$$

where u_d, u_q are the stator voltages; R_s is the stator resistance; i_d, i_q are the stator currents; λ_d, λ_q are the flux linkages and $\omega_{me} = p\,\omega_m$ are the electric speed, pole pairs and mechanical speed, respectively.

The expanded linearized expression of the flux linkages is:

$$\begin{aligned} \frac{d\lambda_d(i_d, i_q)}{dt} &= l_{dd}(i_d, i_q)\frac{di_d}{dt} + l_{dq}(i_d, i_q)\frac{di_q}{dt} \\ \frac{d\lambda_q(i_d, i_q)}{dt} &= l_{dq}(i_d, i_q)\frac{di_d}{dt} + l_{qq}(i_d, i_q)\frac{di_q}{dt} \end{aligned} \tag{2.2}$$

where l_{dd} and l_{qq} are the differential self-inductances and l_{dq} is the differential cross-inductance. Pulsating signal-injection estimates the rotor position by injecting an high frequency sinusoidal voltage signal along the estimated $\widehat{d}$-axis, i.e.:

$$\begin{aligned} \widehat{u}_{hd} &= U_h \cos(\omega_h t) \\ \widehat{u}_{hq} &= 0 \end{aligned} \tag{2.3}$$

where U_h and ω_h are the magnitude and the pulsation frequency of the injected sinusoidal wave. The hat superscript highlights the variables obtained in the $d^x q^x$ reference frame. The different reference frames in which the motor equations can be represented are shown in Fig. 2.1. The measured rotor position ϑ_{me} is defined as the angle between the rotating reference frame dq and the stationary one $\alpha\beta$. The estimated rotor position $\widehat{\vartheta}_{me}$ is the angle between

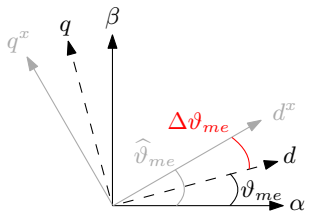

Figure 2.1: Electric motor reference frames: synchronous dq, estimated $d^x q^x$ and stationary $\alpha\beta$.

the estimated $d^x q^x$ reference frame and the $\alpha\beta$ one, whereas $\Delta\vartheta_{me}$ = ϑ_{me} - $\widehat{\vartheta}_{me}$ is the position error.

The injection of an HF voltage signal, leads to induced high frequency currents:

$$\begin{aligned}\widehat{i}_{hd} &= M[l_\Sigma - l_\Delta \cos(2\Delta\vartheta_{me}) - l_{dq}\sin(2\Delta\vartheta_{me})]\sin(\omega_h t)\\ \widehat{i}_{hq} &= M[l_\Delta \sin(2\Delta\vartheta_{me}) - l_{dq}\cos(2\Delta\vartheta_{me})]\sin(\omega_h t)\end{aligned} \tag{2.4}$$

where M = $U_h/(\omega_h(l_{dd}l_{qq}$ - $l_{dq}{}^2))$, l_Δ = $(l_{dd}$ - $l_{qq})/2$ is the differential semi-difference inductance and l_Σ = $(l_{dd}$ + $l_{qq})/2$ is the differential mean value inductance. At the injection frequency the resistive voltage drop is negligible with respect to the inductive one, the motional voltage terms can be neglected due to the low operating speed and the cross coupling terms are neglected as well being $\omega_{me} \ll \omega_h$. The currents in (2.4) represent a pulsating vector $\bar{i}_h$ in the synchronous estimated $d^x q^x$ reference frame as shown in Fig. 2.2. To retrieve the rotor position, the $\widehat{i}_{hq}$ is demodulated with the scheme shown in Fig. 2.3. The estimated currents in the $d^x q^x$ are measured and the high frequency component of the quadrature current $\widehat{i}_q$ is extracted with an High Pass Filter (HPF). The $\widehat{i}_{hq}$ is multiplied for $\sin(\omega_h t)$ and then the signal is filtered with a Low Pass Filter (LPF) to eliminate the alternating component at twice the injection frequency. The signal is then driven to zero by means of the observer. A Proportional Integrator (PI) Regulator (REG), together with the integrator already present in the position observer allow retrieving the estimated rotor position $\widehat{\vartheta}_{me}$.

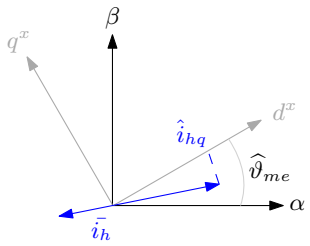

Figure 2.2: Pulsating current vector representation in the estimated reference frame $d^x q^x$.

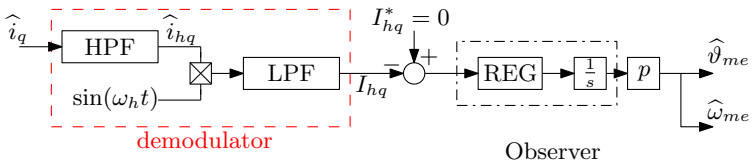

Figure 2.3: Pulsating injection position observer.

2.2 Rotating Signal-Injection

Rotating signal injection retrieve the rotor position by injecting HF voltages in the stationary reference frame $\alpha\beta$. The voltage balance equations of a PMSM in the $\alpha\beta$ reference frame are:

$$\begin{aligned} u_\alpha &= R_s i_\alpha + \frac{d\lambda_\alpha(i_\alpha, i_\beta, \vartheta_{me})}{dt} \\ u_\beta &= R_s i_\beta + \frac{d\lambda_\beta(i_\alpha, i_\beta, \vartheta_{me})}{dt} \end{aligned} \tag{2.5}$$

where u_α, u_β are the stator voltages, i_α, i_β are the stator currents and λ_α, λ_β are the flux linkages. It is worth highlighting the dependency of the flux linkage both on the stator currents and on the rotor position ϑ_{me}. The flux linkages in (2.5) can be written as a function of the motor apparent inductances L_α, L_β and the magnet permanent flux λ_{mg} as:

$$\begin{aligned} \lambda_\alpha(i_\alpha, i_\beta, \vartheta_{me}) &= L_\alpha(i_\alpha, i_\beta, \vartheta_{me}) i_\alpha + \lambda_{mg} \cos(\vartheta_{me}) \\ \lambda_\beta(i_\alpha, i_\beta, \vartheta_{me}) &= L_\beta(i_\alpha, i_\beta, \vartheta_{me}) i_\beta + \lambda_{mg} \sin(\vartheta_{me}). \end{aligned} \tag{2.6}$$

To simplify the notation, in the following equations the explicit stator currents and rotor position will be hidden. Replacing (2.6) in (2.5), the expanded expression of the flux linkages can be found, namely:

$$\begin{aligned} \frac{d\lambda_\alpha}{dt} &= l_\alpha \frac{di_\alpha}{dt} + l_{\alpha\beta} \frac{di_\beta}{dt} + \omega_{me} \left(\frac{dL_\alpha}{d\vartheta_{me}} i_\alpha - \lambda_{mg} \sin(\vartheta_{me}) \right) \\ \frac{d\lambda_\beta}{dt} &= l_\beta \frac{di_\beta}{dt} + l_{\alpha\beta} \frac{di_\alpha}{dt} + \omega_{me} \left(\frac{dL_\beta}{d\vartheta_{me}} i_\beta + \lambda_{mg} \cos(\vartheta_{me}) \right) \end{aligned} \tag{2.7}$$

where l_α, l_β and $l_{\alpha\beta}$ are the motor differential inductances in the stationary reference frame. The differential inductances can be also rewritten as a function of the meaningful differential inductances in the synchronous reference frame defined in 2.4 as follows:

$$\begin{aligned} l_\alpha &= l_\Sigma + l_\Delta \cos(2\vartheta_{me}) - l_{dq} \sin(\vartheta_{me}) \\ l_\beta &= l_\Sigma - l_\Delta \cos(2\vartheta_{me}) - l_{dq} \sin(\vartheta_{me}) \\ l_{\alpha\beta} &= l_\Delta \sin(2\vartheta_{me}) + l_{dq} \cos(2\vartheta_{me}). \end{aligned} \tag{2.8}$$

Rotating injection sensorless techniques [48] add two HF sinusoidal voltage signals on the fundamental ones to excite the system and retrieve the rotor

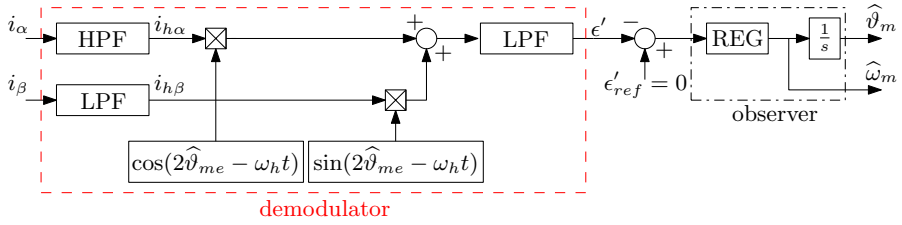

Figure 2.4: Rotating voltage injection system representation.

position. The injected signals are:

$$u_{h\alpha} = U_h \cos(\omega_h t) \qquad u_{h\beta} = U_h \sin(\omega_h t). \tag{2.9}$$

The injected voltages induce HF currents in the stationary reference frame $\alpha\beta$:

$$\begin{aligned} i_{h\alpha}(t) &= I_s(l_\Sigma \sin(\omega_h t) + \sqrt{l_\Delta^2 + l_{dq}^2}\sin(2(\vartheta_{me} - \epsilon) - \omega_h t)) \\ i_{h\beta}(t) &= -I_s(l_\Sigma \cos(\omega_h t) + \sqrt{l_\Delta^2 + l_{dq}^2}\cos(2(\vartheta_{me} - \epsilon) - \omega_h t)) \end{aligned} \tag{2.10}$$

where I_s = $U_h/(\omega_h(l_{dd}l_{qq}$ - ${l_{dq}}^2))$ and ϵ= $0.5\,\text{atan2}(\text{-}l_{dq},l_\Delta)$ is the steady state open loop estimation error due to the cross differential effects. A more detailed explanation of the meaning of ϵ will be given in Section 2.2.2. The currents in (2.10) are composed by two components, the positive sequence does not contain information about the rotor position while the negative sequence can be used to obtain the information about the rotor position. A system representation for rotating signal injection is shown in Fig. 2.4. To retrieve the rotor position, the measured stator currents in the stationary reference frame $\alpha\beta$ are filtered by means of an HPF to isolate the high frequency components. The HF currents $i_{h\alpha}$ and $i_{h\beta}$ are multiplied for co-sinusoidal functions that depend both on ω_h and the estimated rotor position $\widehat{\vartheta}_{me}$. The signals are then added together and the resulting signal is filtered by a LPF to eliminate the oscillating component at twice the injection frequency added by the demodulation. The output of the demodulator block ϵ' is:

$$\epsilon' = I_s\sqrt{l_\Delta^2 + l_{dq}^2}\sin(2(\vartheta_{me} - \widehat{\vartheta}_{me} - \epsilon)) \approx 2I_s\sqrt{l_\Delta^2 + l_{dq}^2}(\vartheta_{me} - \widehat{\vartheta}_{me} - \epsilon) \tag{2.11}$$

where a small estimation error is assumed to approximate the sine function with its argument. A PI, together with the integrator already presents in the observer scheme, is able to retrieve the estimated rotor position.

2.2.1 Ellipse Fitting

Ellipse fitting technique [49,50] is a sensorless technique based on the imposition of two HF signals in the stationary reference frame. The process to retrieve

the rotor position is an alternative to the demodulation scheme described in Section 2.2. The HF voltages induce HF currents, whose trace in the stationary $\alpha\beta$ reference frame is an ellipse. The ellipse rotates at the electrical motor speed ω_{me} accordingly to the rotor position.

The information about the rotor position is contained in its major axis tilt that is oriented with the rotor axis with lower inductance, i.e. d-axis for IPM and q-axis for SynRM. The tilt of the ellipse is retrieved from the sampled currents with a Recursive Least Square (RLS) algorithm by using the implicit equation of the ellipse, namely:

$$ai_\alpha^2 + bi_\alpha i_\beta + ci_\beta^2 + di_\alpha + ei_\beta = f \tag{2.12}$$

where $\Theta = [a, c, b, d, e, f]^T$ is the vector of coefficients that describes an ellipse in the $\alpha\beta$ reference frame. It is worth noting that in (2.12) the current samples are composed by the fundamental currents (i_α,i_β) and the HF ones ($i_{h\alpha}$,$i_{h\beta}$). Therefore, the currents samples are not filtered by an high pass filter as the conventional ellipse fitting algorithms [51]. The high pass filter is not able to track the ellipse trajectory centered on the origin during transient. As a consequence the rotor position estimation is worsened.

The relationship between the ellipse coefficients Θ and the motor parameters is:

$$\begin{aligned}
a &= l_\Sigma^2 + l_\Delta^2 + l_{dq}^2 + 2l_\Sigma\sqrt{l_\Delta^2 + l_{dq}^2}\cos(2(\vartheta_{me} - \epsilon)) \\
b &= 4l_\Sigma\sqrt{l_\Delta^2 + l_{dq}^2}\sin(2(\vartheta_{me} - \epsilon)) \\
c &= l_\Sigma^2 + l_\Delta^2 + l_{dq}^2 - 2l_\Sigma\sqrt{l_\Delta^2 + l_{dq}^2}\cos(2(\vartheta_{me} - \epsilon)) \\
d &= -(2aI_\alpha + bI_\beta) \\
e &= -(2cI_\alpha + bI_\alpha) \\
f &= \frac{U_h^2}{\omega_h^2} - aI_\alpha^2 - bI_\alpha I_\beta - cI_\beta^2.
\end{aligned} \tag{2.13}$$

It is worth noting the dependency from the motor parameters of the coefficients $[a, b, c]$, whereas $[d, e]$ also depends on the fundamental currents. Furthermore, provided that the ellipse trace is detectable, the ellipse tilt is independent to the current magnitude. The estimated rotor position can be retrieved by manipulating the estimated coefficients $[a, b, c]$, namely:

$$\widehat{\vartheta}_{me} = \frac{1}{2}\operatorname{atan}\frac{b}{a - c}. \tag{2.14}$$

The estimated position with (2.14) it is not used in a real electric drive with ellipse fitting algorithm due to two main flaws. The former one is that, due to the ellipse symmetry over π, the estimated position varies only in the range of $[0, \pi]$. The latter is that it is a noisy estimation since it is retrieved from trigonometric functions with estimated coefficients as argument. A smoother

estimation with a proper range can be obtained by computing the sine and cosine functions of $\widehat{\vartheta}_{me}$, namely:

$$\begin{aligned} \cos(2\widehat{\vartheta}_{me}) &= \frac{a-c}{\sqrt{b^2+(a-c)^2}} \\ \sin(2\widehat{\vartheta}_{me}) &= \frac{b}{\sqrt{b^2+(a-c)^2}}. \end{aligned} \tag{2.15}$$

The estimator uses the sine and cosine components to feed a Quadrature-PLL ($Q-PLL$) shown in Fig. 2.5. It is worth noting that the unitary gain between the estimated position from the $Q-PLL$ and by means of the RLS algorithm is neglected to ease the notation. The regulator inside the $Q-PLL$ scheme can be easily tuned since its closed-loop transfer function is:

$$W(s) = \frac{REG(s)}{s+REG(s)} \tag{2.16}$$

where no parameters appear.

Finally, it is worth noting than no motor parameters are used to retrieve the rotor position or to tune the estimator, so the chosen observer can be considered robust against parameter mismatches. The regulator tuning is a crucial point in a sensorless drive since the performance of the position estimator strictly depends on its tuning. Fast and stable position estimation and an high disturbance rejection are the key point that must be guaranteed during the design of the regulator. Model based design method needs the motor parameters to tune the regulator. However the described method does not require any motor parameters knowledge. The RLS algorithm elaborates the measured currents, by minimizing he sum of the squared distance between the measured currents and the fitting model, the best ellipse parameters are estimated. Hence, no motor data are required. This is an important characteristic compared to other conventional observers where motor parameters knowledge are mandatory to guarantee a constant observer open-loop gain and, in turn, constant performance [52]. The EF algorithm together with the $Q-PLL$ form the Position Estimator (PE).

A feasible regulator to retrieve the rotor position could be a PI controller. A critical damping factor $\xi_{pll} = 1/\sqrt{2}$ and a desired natural pulsation ω_{pll} have to be chosen for the regulator tuning. Selecting the critical damping factor is a design choice and typically its choice needs to take into consideration a slow response of the estimation after accelerations. The aforementioned requirement can be achieved by means of the following proportional K_p and integral K_i coefficients:

$$\begin{aligned} K_p &= \sqrt{2}\omega_{pll} \\ K_i &= \omega_{pll}^2 \end{aligned} \tag{2.17}$$

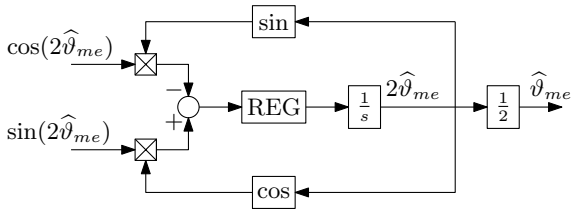

Figure 2.5: Quadrature-PLL scheme.

2.2.2 Self-Sensing Capability

High frequency injection is based on the addition of HF signals on the fundamental one. The estimated rotor position $\widehat{\vartheta}_{me}$ is retrieved by analyzing the response of the motor according to the sensorless algorithm used. The feedback of the motor is a function of its own parameters, i.e., the depicted anisotropy. Hence, a motor can be more suitable for sensorless control than another one [53, 54]. The ability of the motor to be controlled without position sensor is referred as the self-sensing capability. Indeed, the motor itself acts as a sensor in a sensorless drive.

Magnetic saturation and cross-coupling negatively affect sensorless control. T he former reduces the detectable anisotropy whereas the latter one induces a position estimation error ϵ which degrades the electric drive performance and it could lead to stability issues. At steady state, the relationship between $\widehat{\vartheta}_{me}$ and the estimation error is the following:

$$\widehat{\vartheta}_{me}(i_d, i_q) = \vartheta_{me} + \epsilon(i_d, i_q) \tag{2.18}$$

where ϵ can be computed as:

$$\epsilon(i_d, i_q) = 0.5 \operatorname{atan2}(l_{dq}(i_d, i_q), -l_{\Delta}(i_d, i_q)). \tag{2.19}$$

A more detailed definition of the differential inductances in the dq reference frame is the local derivative of the flux linkage maps:

$$\begin{bmatrix} l_{dd}(i_d, i_q) & l_{dq}(i_d, i_q) \\ l_{qd}(i_d, i_q) & l_{qq}(i_d, i_q) \end{bmatrix} = \begin{bmatrix} \frac{\partial \lambda_d(i_d, i_q)}{\partial i_d} & \frac{\partial \lambda_d(i_d, i_q)}{\partial i_q} \\ \frac{\partial \lambda_q(i_d, i_q)}{\partial i_d} & \frac{\partial \lambda_q(i_d, i_q)}{\partial i_q} \end{bmatrix}. \tag{2.20}$$

It is worth noting that the estimation error depends on the the operating point of the machine since saturation and cross-saturation inductance vary according to the current operating point. At low current cross-saturation inductance is usually negligible and, in turn, the estimation error. As the current increases ϵ becomes more relevant.

The motor self-sensing capability can be studied by defining the observer trajectories. The observer trajectories are defined as sensored trajectory t_1 and sensorless trajectory t_2. To depict them, an estimator can be implemented to estimate the rotor position. To obtain the t_1 trajectory, the control is closed on

the measured position, i.e., the estimator works in open loop. Therefore, the estimated rotor position is not used in the control and ϵ does not affect the operating point of the machine. As a consequence, if the control loops are well designed, the actual operating point coincides with the reference one. The estimation error can be computed for any current level along a predetermined Reference Trajectory (REF) and it can be depicted in the dq current plane by:

$$\begin{aligned} i_d^x &= i_d \cos(\epsilon(i_d, i_q)) - i_q \sin(\epsilon(i_d, i_q)) \\ i_q^x &= i_d \sin(\epsilon(i_d, i_q)) + i_q \cos(\epsilon(i_d, i_q)) \end{aligned} \tag{2.21}$$

where i_d and i_q are obtained with the measured position and i_d^x and i_q^x depict the desired trajectory in the estimated reference frame. It is worth noting that the trajectory t_1 exists for any level of current load, since the drive is not affected by the observer and, in turn, by its estimation error. The angle between the reference line and t_1 represents the estimation error. At low load, magnetic cross-saturation is almost negligible, so ϵ is negligible as well, whereas it increases as the current magnitude raises to its nominal value since magnetic saturation and cross-coupling become relevant. It is worth highlighting that the electric drive does not work in every condition along the sensored trajectory t_1 since it is only a graphical expedient to show the observer's estimation error for any load level.

In a sensorless electric drive, the estimated position is used to perform Park transformation and to compute the speed feedback. The estimator operates in closed loop, hence its performance and accuracy affect the overall electric drive behaviour. In sensorless mode, the motor draw a different trajectory that is called t_2 and can be calculated with (2.21). In this condition even i_d and i_q are affected by the estimation error since the whole electric drive is closed on the estimated position. The trajectory t_2 represents the electric drive operating locus in sensorless mode computed from a reference trajectory. The trajectory t_2 does not exist for any current level, since if the estimation error is too large, no stable points exist for the overall system, leading the electric drive in unstable condition. Stable points around t_2 can be found by computing the intersection between the condition where the high frequency currents are zero and their derivate with respect the current angle has negative slope [55,56].

3 Investigation on the Self-Sensing Capability of a Dual Three-Phase Synchronous Reluctance Machine

An investigation on the self-sensing capability of a dual three-phase synchronous reluctance motor is proposed in this chapter. Low speed sensorless algorithms retrieve the rotor position by exploiting the motor anisotropy, which must be detectable. However, magnetic saturation and magnetic cross-coupling negatively affect the performance of the estimator. IPM and SynR motors are suitable for estimating the rotor position by means of low speed sensorless algorithms due to their relevant rotor anisotropy but, at the same time, they exhibit a strong magnetic saturation which effect must be properly evaluated.

As highlighted in Section 2.2.2, an estimation error is introduced by sensorless control. An expression to calculate ϵ is reported in (2.19). It is worth remembering the dependency of ϵ from the operating point of the machine. At low load, magnetic cross-saturation is almost negligible and ϵ is negligible as well, whereas it increases as the current magnitude raises to its nominal value since magnetic saturation and cross-coupling become relevant. Sensorless control divergence can occur when the motor is highly saturated due to the high value of ϵ. To study the operating points in the dq plane in which sensorless control can be performed, self-sensing capability has been introduced. Sensored trajectory t_1 allow depicting the Open Loop (OL) estimation error, whereas sensorless trajectory t_2 describes the stable operating points where a motor can be controlled sensorless.

By means of the study on the self-sensing capability, a sensorless control strategy for the aforementioned motor is developed. The multiphase machine is decomposed and studied as two different three-phase systems according to the MS approach. The two three-phase sets are controlled by two different inverter, hence they can operate at different operating points. The additional degree of freedom given by the second three-phase winding is used to enhance the fault-tolerant capability of the motor by performing sensorless control.

The reference scenario is a fault in the position sensor. In case of mechanical sensor fault, a three-phase winding is controlled at low current and high frequency signals are injected to retrieve the rotor position. The reduced magnetic saturation due to the working condition allows achieving an accurate rotor position estimation which is used by both windings of the machine. The second three-phase winding can work until its nominal current and overloaded. For the sake of clarity it is worth noting that a reduction of the torque available at the rotor shaft is obtained with the proposed sensorless technique. Normally, if the current in one winding set is reduced, an increase

Table 3.1: Summary of the experimental tests.

Test	Brief description	Key points
Three-phase Configuration	Motor operates as a three-phase machine	FEA simulation and experimental results are akin to each other
Half-Control: HC-mode	Only one winding is enabled	Trajectories t_1 and t_2 overlap for low current values: no ϵ in this condition
Six-Phase Control: part 1	xyz set closed on ϑ_{me} and operating at different operating points along REF	Self-sensing capability of the abc set improved when the xyz one operate at high current
Six-Phase Control: part 2	xyz set closed on $\widehat{\vartheta}_{me}^{xyz}$ and operating at different operating points along REF	Results of Six-Phase Control: part 1 confirmed and perfect match between sensored mode and complete sensorless mode
Six-Phase Control: part 3	xyz set closed on $\widehat{\vartheta}_{me}^{xyz}$ and operating at different operating points along REF	Motor dragged at fixed speed and abc winding able to operate up to its nominal current without sensorless control divergence and negligible ϵ

of the current in the second set is obtained to operate at constant torque. However this is not the case since a torque reduction is necessary to allow estimating the correct rotor position. As a consequence it is true that the proposed control algorithm reduces the motor performance. On the other hand, it allows operation in case of a mechanical sensor fault without changing the control technique or applying complex compensation methods. As a result, the fault-tolerant capability of the motor is enhanced. Moreover, the estimated position is accurate and not affected by the estimation error due to cross-magnetic saturation that is the main flaw of low speed algorithm and no motor parameters are required.

Several supply scenarios are studied where the two three-phase windings are controlled at different operating points along a reference current trajectory in the dq plane. All the tests and the results are summarized for more clarity in Tab. 3.1. In the three-phase configuration the two three-phase sets are closed in series resulting in a three-phase configuration. In the Half-Control (HC) mode, only one set is supplied whereas the second one is disabled. During the six-

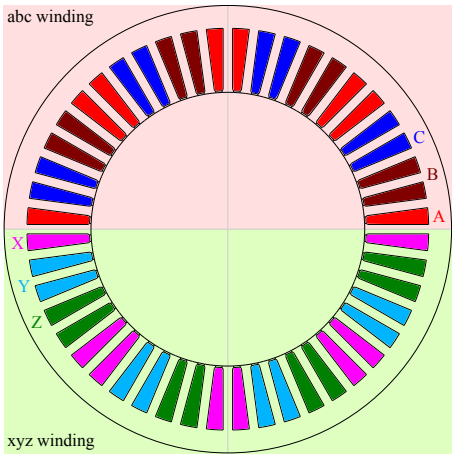

Figure 3.1: Adopted layout of the stator windings. One three-phase system is distributed at the top of the stator, the latter one at the bottom.

phase control, both sets are supplied. The analysis is carried out both with FEA simulations and experimental tests. Several results will show the comparison between simulated and experimental tests to highlight the effectiveness of the proposed study. In the following, motor description and modelling is reported in Section 3.1. The adopted sensorless control strategy is described in Section 3.2. Results and observer trajectories are thoroughly discussed in Section 3.3. Finally, the conclusion and novelty of the reported study are illustrated in Section 3.4.

3.1 Motor Description and Modelling

A machine with six phases is studied. The stator of the motor is split into two identical three-phase windings labeled as abc and xyz where each electrical system is supplied by a dedicated inverter. The former one is distributed at the top of the stator, whereas the latter one at the bottom as shown in Fig. 3.1. The two winding sets do not have any angular shift, they are aligned as shown in Fig. 3.2. The layout employed reduces the mutual inductances between the two windings, improving the fault-tolerant capability [57, 58]. One winding can be supplied, even if the other one is short-circuited, namely, HC mode.

The winding arrangement is reported in Fig. 3.3. The chosen configuration is the so called W-11-22. Tab. 3.2 shows the main data of the motor, whereas further details of the motor design, the thermal analysis under fault operating conditions and its flux weakening capabilities can be found in [59, 60].

FEA and experimental tests are performed to characterize the motor. Flux linkage maps and torque are calculated in the dq plane for different supply scenarios in which the motor will be supplied during the experimental tests. Magnetic maps are measured with a constant speed method and both

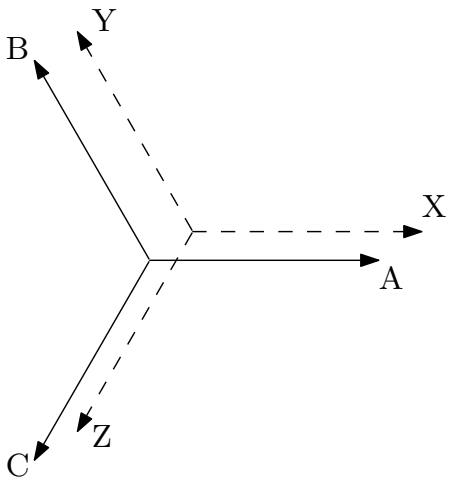

Figure 3.2: Winding shift of the adopted stator configuration.

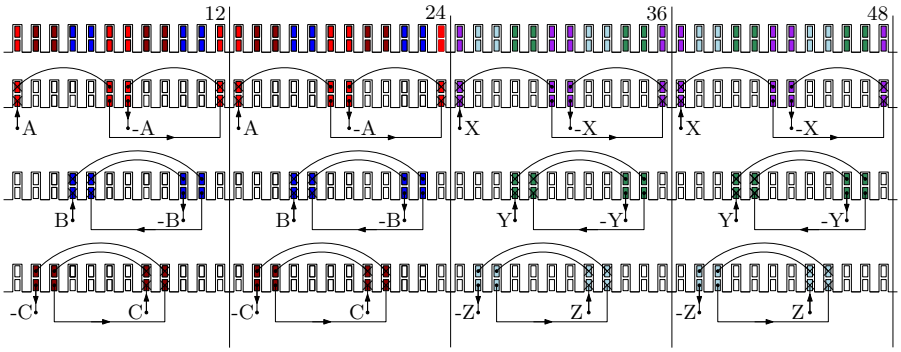

Figure 3.3: W-11-22 winding arrangement.

windings are fed with the current vector imposed in the dq plane [61]. In the following, firstly the three-phase configuration is analyzed, then the HC mode.

3.1.1 Three-Phase Configuration

In three-phase configuration both windings are connected in series and supplied with the same current. Flux linkage maps are obtained both through FEA simulations and experimental measurements. The results are depicted in Fig. 3.4. Simulated results are akin to the measured one along both d and q-axis in the rotating reference frame. A slightly difference occurs when the motor is heavily saturated.

3.1.2 Half-Control Condition

Only the abc winding is supplied during HC-mode. The motor is controlled as a single three-phase system and supplied by only one inverter. The xyz

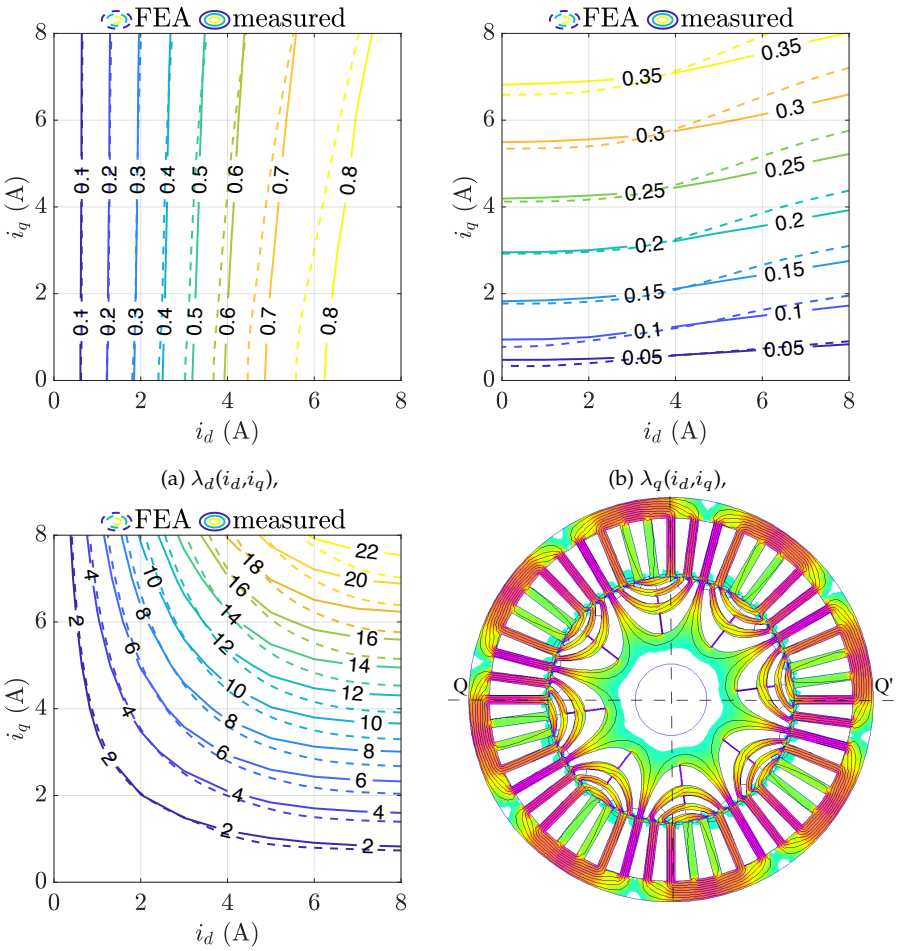

(a) $\lambda_d(i_d,i_q)$,

(b) $\lambda_q(i_d,i_q)$,

(c) Torque,

(d) Flux density plot,

Figure 3.4: Flux density plot, linkage maps and torque comparison between measured and FEA simulations in three-phase configuration.

Table 3.2: Geometric motor data.

Parameter	Symbol	Value
Stack length	L_{stk}	85 mm
Number of slots	Q	46
Series conductor per slot	n_c	46
Parallel conductor per slot	n_p	1
Slot fill factor	k_{fill}	0.4
Air gap	g	0.4 mm
Outer diameter	D_e	170 mm
Inner diameter	D_i	104 mm
Tooth width	w_t	3.6 mm
Slot height	h_s	24.3 mm
Number of barriers	n_b	3

winding is completely open, hence no voltages and currents are applied to it. This is a particular scenario in which the motor can operate, for instance during a fault in the second three-phase winding. Fig. 3.5a and Fig. 3.5b shows the flux linkage maps $\lambda_d^{abc}(i_d,i_q)$ and $\lambda_q^{abc}(i_d,i_q)$ calculated through FEA simulations. The superscript on a variable means that the quantity refers to the indicated three-phase system. Same results can be obtained by supplying only the xyz winding.

The torque map during the HC-condition is depicted in Fig. 3.5c. The maps show that the magnetisation of the motor is not homogeneous and symmetric. Flux density plot for the HC-mode when the mechanical rotor position $\vartheta_{me} = 0\,\mathrm{rad}$ is depicted in Fig. 3.5d. Flux lines flow in the stator area of the open xyz three-phase system, reducing the flux linkage in the supplied three-phase winding. The zero-value torque level is rotated with respect to the dq-current plane axes since the magnetic flux produced by the supplied three-phase winding is not bounded in the active region. In HC condition, the d and q-axis flux linkage are not null even if the d or the q-axis currents are zero, respectively, namely, $\lambda_d^{abc}(0,i_q) \neq 0$ and $\lambda_q^{abc}(i_d,0) \neq 0$. This aspect is reflected in the torque map, indeed non-zero torque value is reported along the dq-current axes. It is an unconventional behaviour for a synchronous reluctance machine if compared to the flux density plot obtained for the three-phase configuration in Fig. 3.4d. It is worth reminding that the chosen winding configuration minimises the mutual coupling between the two electrical systems and, in turn, the induced current in case of a short-circuit in one of three-phase system, but exhibits this non-conventional behaviour in case of open circuit fault.

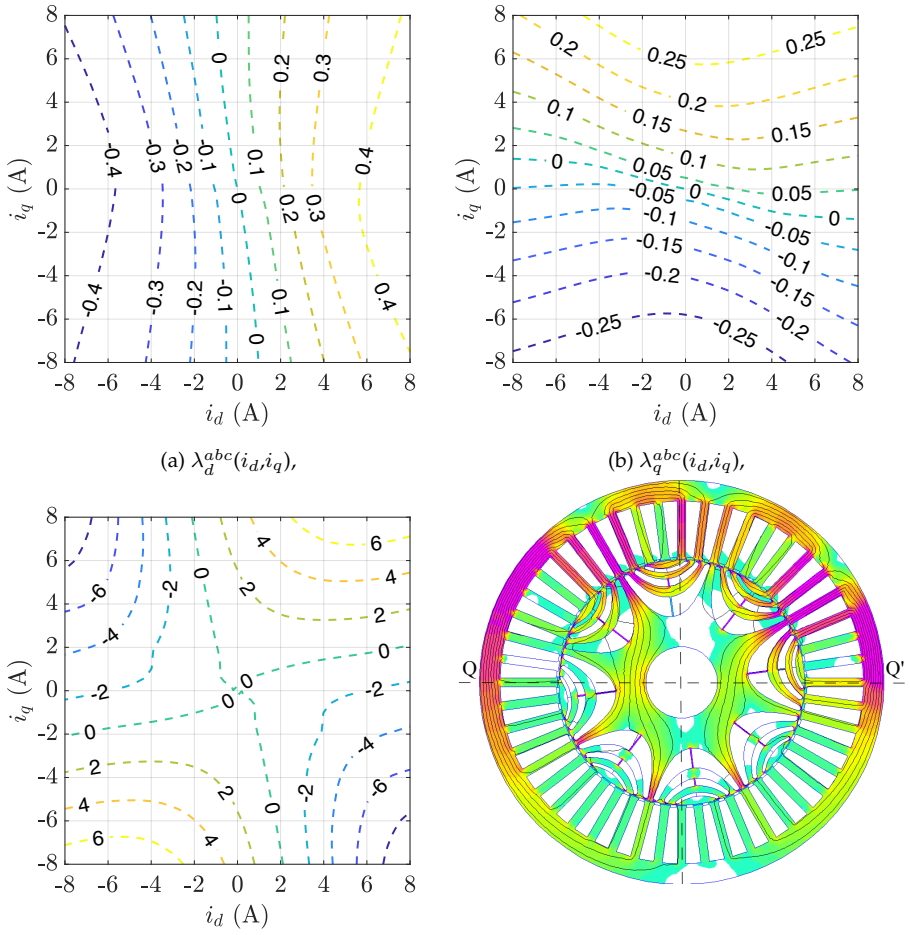

(a) $\lambda_d^{abc}(i_d,i_q)$,

(b) $\lambda_q^{abc}(i_d,i_q)$,

(c) Torque,

(d) Flux density plot,

Figure 3.5: Flux density plot, linkages maps obtained through FEA simulations in half condition mode (only the abc set is supplied).

3.2 Sensorless Strategy

Sensorless control strategy implemented in this analysis has been discussed in Section 2.2.1. An estimation algorithm is implemented in each winding sets, resulting in two estimated positions $\widehat{\vartheta}_{me}$. It is worth remembering that as explained in Section 2.2.1, the selected estimation algorithm requires no motor parameters knowledge for the position estimation, so it is inherently robust against parameter mismatches.

To close the current control loop, the high frequency currents in the rotating reference frame are filtered by means of a LPF. The filtered currents i_d and i_q are then used as feedback and compared to the reference ones i_d^* and i_q^*. PI controllers are designed to drive the error to zero and calculate the fundamental reference voltages. Fig. 3.6 shows the adopted scheme for the motor control and position estimation for a single three-phase system. As highlighted the Control (CTRL) part is composed by:

- a current control loop implemented with PI controllers. They are designed to achieve $100\,\mathrm{Hz}$ bandwidth with a phase margin of $70°$. The feedback currents can be computed with the measured position ϑ_{me} (switch in 1) or with the estimated one $\widehat{\vartheta}_{me}$ (switch in 2);
- The high frequency signals injection in the $\alpha\beta$ stationary reference frame to retrieve the rotor position;
- The pulse width modulation inverter;
- A low pass-filter to retrieve the main components from measured currents.

The position estimator is reported as well and it is composed by:

- The Ellipse Fitting (EF) algorithm that retrieves the rotor position;
- A $\mathrm{Q}-\mathrm{PLL}$ that smooth the estimated quantity.

3.3 Results

The proposed sensorless control strategy and the self-sensing capability of the Motor Under Test (MUT) are verified throughout an extensive experimental stage. The MUT is a dual-three phase synchronous reluctance motor, whose parameters are reported in Tab. 3.3. The injection quantities are listed in Tab. 3.4. The sampling frequency is equal to the switching one at $10\,\mathrm{kHz}$. The test bench is shown in Fig. 3.7. The MUT is coupled to a $4.5\,\mathrm{kW}$ PMSM which is supplied by its own inverter. The PMSM, namely, master motor, enables to drag the MUT at a fixed speed. The MUT is controlled along a

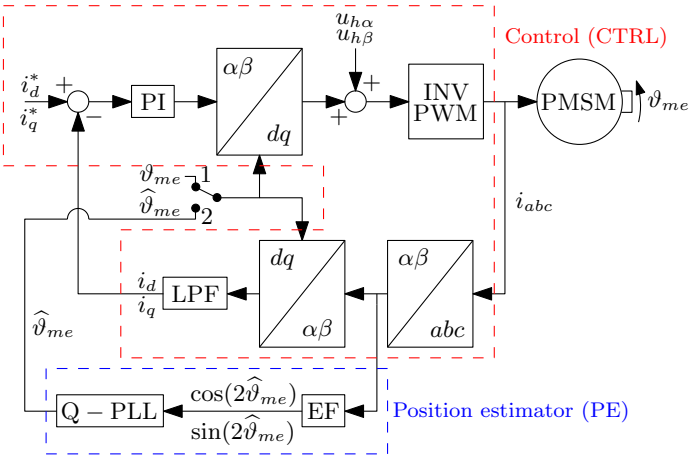

Figure 3.6: Current control loop and position estimator scheme with rotating injection in $\alpha\beta$ and ellipse fitting technique. The scheme is implemented for both windings. The system operates in sensored mode when the switch is in position 1, otherwise it operates in sensorless mode.

Table 3.3: Plate data of the motor under test.

Parameter	Symbol	Value
Rated voltage	V_N	350 V
Rated speed	ω_N	1000 rpm
Pole pairs	p	4
Nominal current	I_N	8.3 A
Nominal torque	T_N	14 N m

reference trajectory and each three-phase winding is supplied by its own inverter. The control algorithm is implemented on a dSpace MicroLabBox platform connected to the host PC. Current controllers are designed to achieve a bandwidth of 100 Hz.

For a better understanding of the signals used to calculate the observer trajectories of the load winding and the position used to close the control loop of the estimation one, a summary is reported in Tab. 3.5. Three-phase test is excluded since the motor is treated as an unique three-phase system. In this case the measured position is used for the calculation of the sensored t_1

Table 3.4: Sensorless drive parameters.

Parameter	Symbol	Value
Injection magnitude	U_h	100 V
Injection frequency	f_h	1000 Hz

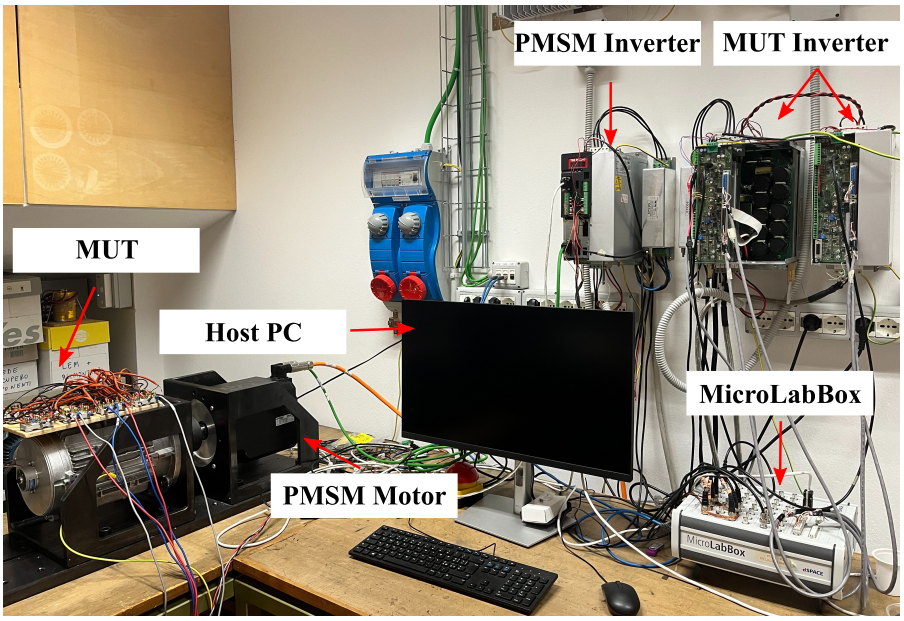

Figure 3.7: Test bench experimental setup.

trajectory, whereas only one estimator is implemented. As a consequence, the estimated position is used for the calculation of the sensorless trajectory t_2.

Five different tests are carried out to study the self-sensing capability of the motor and to verify the effectiveness of the proposed method. The first test is aimed to study the self-sensing capability of the motor when the two three-phase windings are connected in series. In this scenario the motor is supplied by only one inverter, namely, in three-phase configuration. This test is reported in Section 3.3.1. The second test investigates the HC-mode, hence only one winding is supplied and the other one disconnected. This scenario is reported in Section 3.3.2. The interaction between the two three-phase systems and its effect on the self-sensing capability is investigated in Section 3.3.3 by controlling the two three-phase windings in different operating points. The condition where both three-phase sets are supplied with different control strategies by two separate inverter is hereafter called six-phase control. In Section 3.3.4, the control loops of both windings are closed on the estimated position obtained from the electrical system operating at low current along REF. These tests are implemented at locked rotor $\vartheta_{me} = 0\,\mathrm{rad}$, namely, at standstill condition. In Section 3.3.5 the MUT is coupled to a PMSM and dragged at $50\,\mathrm{rpm}$ to test the effectiveness of the control strategy developed in Section 3.3.4 at low speed.

Table 3.5: Summary of the experimental tests.

Test	xyz winding closed on	abc winding closed on
Half-Control: HC-mode	disabled	Locked rotor. t_1: ϑ_{me}, t_2: $\widehat{\vartheta}_{me}^{abc}$
Six-Phase Control: part 1	ϑ_{me} and operating at different Constant Operating Points (COP)	Locked rotor. t_1: ϑ_{me}, t_2: $\widehat{\vartheta}_{me}^{abc}$
Six-Phase Control: part 2	$\widehat{\vartheta}_{me}^{xyz}$ and operating at different Constant Operating Points (COP)	Locked rotor. t_1: $\widehat{\vartheta}_{me}^{xyz}$, t_2: $\widehat{\vartheta}_{me}^{abc}$
Six-Phase Control: part 3	$\widehat{\vartheta}_{me}^{xyz}$ and operating at low current	Motor dragged. abc set closed on $\widehat{\vartheta}_{me}^{xyz}$. No trajectories calculation since the motor is rotating but operation in complete sensorless mode

3.3.1 Three-Phase Configuration

Both three-phase sets are connected in series to operate the motor in three-phase configuration. The result is a single three-phase machine, therefore an unique estimator is used to retrieve the rotor position. The layout of the experiment is shown in Fig. 3.8.

When the switch is in position 1, the current control operates with the actual measured position and the estimated one is exploited to compute the sensored trajectory t_1. With the switch in position 2, the CTRL is closed on the estimated position and the electric drive operates in the estimated rotating reference frame, so the sensorless trajectory t_2 can be obtained.

Fig. 3.9 shows the comparison between the trajectories measured during

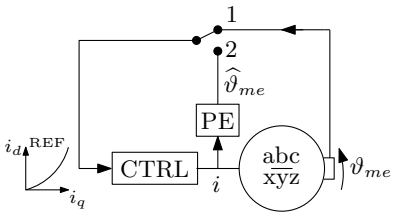

Figure 3.8: Block scheme of the experiment during the three-phase configuration. When the switch is closed on position 1 the motor operates in sensored mode, otherwise it operates sensorless. The MUT follows a ramp-wise reference REF.

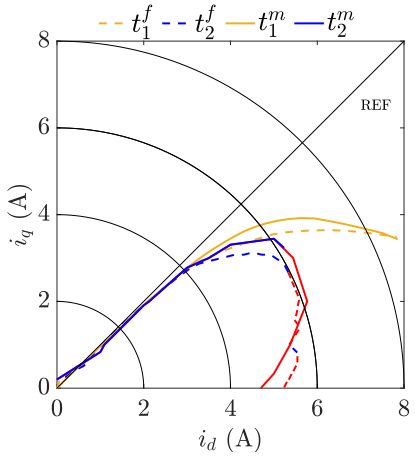

Figure 3.9: Observer trajectories comparison between measured (t_1^m,t_2^m) and simulated (t_1^f,t_2^f) ones when the motor operates as a three-phase system. Unstable points around the trajectory t_2 are highlighted in red line.

the experimental test (t_1^m,t_2^m) and computed by FEA magnetic maps (t_1^f,t_2^f). The theoretical trajectories are obtained by using the Apollo software [62]. Experimental and simulated results look very similar. For current magnitude lower than 4 A, the estimation error is almost negligible being t_1 overlapped to the reference. The sensorless trajectory t_2 is overlapped as well, since estimation error does not affect the electric drive. For higher current values, an estimation error appears and it affects the sensorless operation. The trajectory t_2 starts to diverge, according to the analysis carried out in Section 2.2.2. For current values higher than 5.5 A, the system becomes unstable since the open loop estimation error is quite large (see t_1) and a convergence point does not exist for the observer. It is worth highlighting that not all the points around t_2 are stable. Indeed the points both in red line both for FEA and experimental measurement represents the unstable points around the sensorless trajectory as discussed in Section 2.2.2.

3.3.2 Half-Control

In HC-mode, only one three-phase system is supplied. A schematic of the experiment is shown in Fig. 3.10. The observer trajectories are calculated as in the previous test. The comparison between the experimental and simulated observer trajectories is shown in Fig. 3.11. The measured and the simulated observer trajectories are comparable. A slight difference can be noted at low current where the simulated trajectories are overlapped but not with the reference and the measured one. The current value at which the trajectories are overlapped is the same both for experimental and simulated results and it is equal to 3 A.

At higher current values, the sensored trajectories t_1^m and t_1^f are almost the

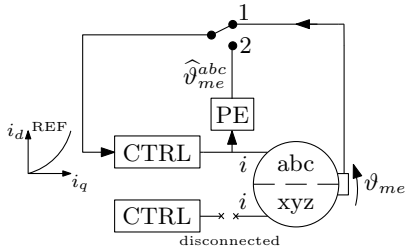

Figure 3.10: Block scheme of the experiment during the HC-condition. The abc winding is supplied, the xyz one disconnected.

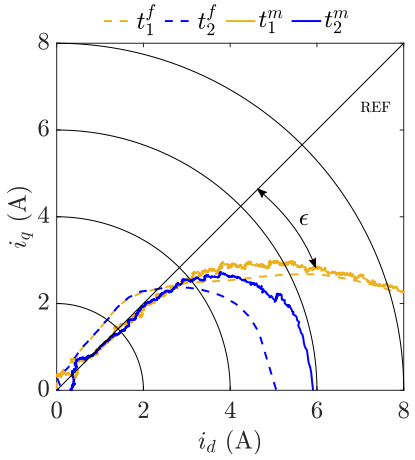

Figure 3.11: Observer trajectories comparison between measured (t_1^m,t_2^m) and simulated (t_1^f,t_2^f) analysis when the motor operates in HC-mode.

same. The simulated sensorless trajectory t_2^f exhibits convergence issue for current values close to 4.5 A. Whilst, the measured sensorless trajectory t_2^m is slightly wider than the simulated one, showing that real operational limit for sensorless operation is slightly higher.

In the following tests, the xyz winding is controlled at Constant Operating Points (COP) whereas the abc one follows a ramp-wise current reference, as in previous tests. Additional high-frequency signals are injected in both windings to estimate the rotor position. The estimated rotor position with the abc winding is used to study the self sensing capability of the motor and trace the trajectory t_1 and t_2 whereas the xyz estimated rotor position is exploited to compute the Park transformation in the closed-loop control. For this reason, the abc winding is called *load* one and the xyz one is referred as *estimation* winding.

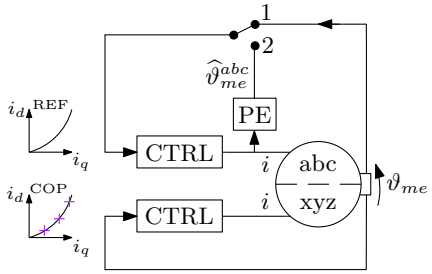

Figure 3.12: Six-phase control: part 1 block scheme of the experiment. The estimation winding is supplied and operate at constant operating points along REF. Its control loop is closed on the measured position during both observer trajectories calculation of the load winding.

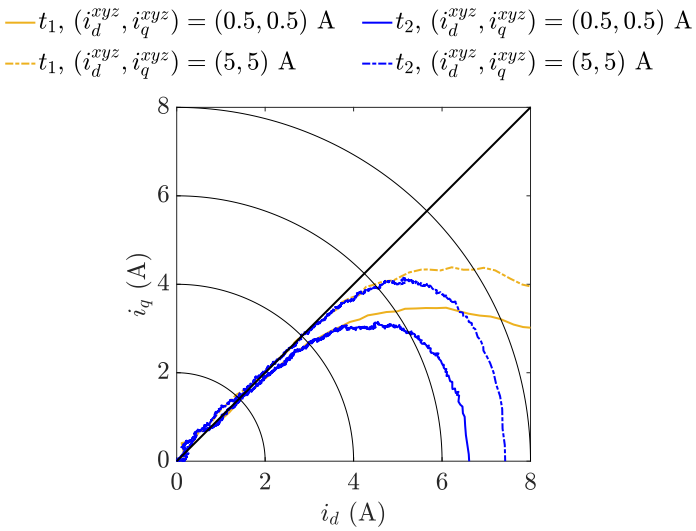

Figure 3.13: Six-phase control: part 1. Load winding observer trajectories when the estimation winding operates at COP. Its control loop is closed on the measured position for both the load winding observer trajectories calculation.

3.3.3 Six-Phase Control: part 1

This test investigates the effects of the operating point of the estimation winding on the self-sensing capability of the load one. t_1 and t_2 are calculated by implementing the PE in the load winding as in the previous tests but the estimation one is supplied and it operates at COP. Moreover, the estimation winding control loop is closed on the measured position. A block scheme of the experiment is depicted in Fig. 3.12. The results of the experiments are shown in Fig. 3.13 where two operating points are evaluated for the estimation winding, namely, (i_d^{xyz},i_q^{xyz}) = (0.5 A, 0.5 A) and (5 A, 5 A).

The self-sensing capability of the load winding is improved in the second case indeed both trajectories t_1 and t_2 follow the reference line for a larger seg-

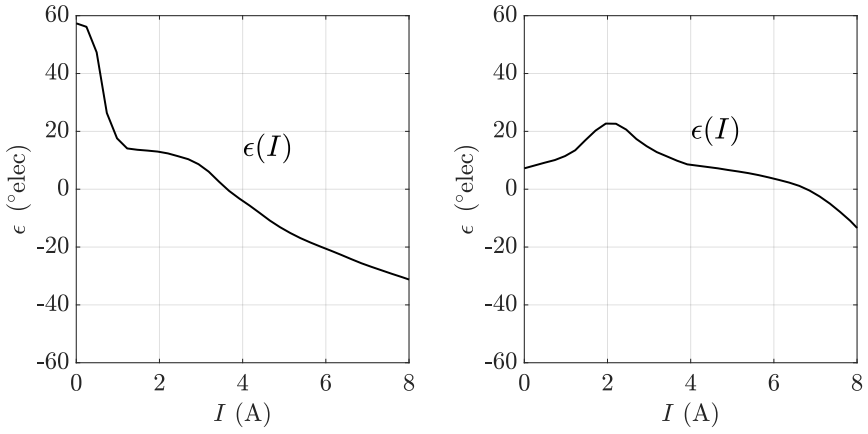

(a) $(i_d^{xyz}, i_q^{xyz}) = (0.5, 0.5)$ A, (b) $(i_d^{xyz}, i_q^{xyz}) = (5, 5)$ A,

Figure 3.14: Six-phase control: part 1. Open loop estimation error of the load winding. The estimation one is supplied at COP and its control loop closed on the measured position.

ment and the sensorless trajectory becomes unstable at a higher current level. It is worth remembering that when the sensored and sensorless trajectories overlap with the reference, no estimation error is detected.

FEA analysis is carried out to investigate the obtained results. The open source package Apollo, which is part of Dolomites software, is used to calculate the estimation error of the load winding in the same scenario experimentally analysed and results are shown in Fig. 3.14. A plateau can be recognised from 4 A to 6 A when the estimation winding operates at 5 A. In this range, the estimation error of the load winding is lower than the 0.5 A load winding operating condition. It is worth noting that the plateau is located where the self-sensing capability of the machine increases in accordance with the experimental evidences.

3.3.4 Six-Phase Control: part 2

In the test described in Section 3.3.3, a negligible estimation error is observed with the estimation winding partially loaded indeed both sensored and sensorless trajectories overlap the reference one. This test exploits previous results and verifies the self sensing capability of the motor in complete sensorless operating mode. The measured rotor position is used only for checking the estimation accuracy. The estimation winding is controlled to a low current COP as a negligible estimation error is obtained. The estimated rotor position $\widehat{\vartheta}_{me}^{xyz}$ is used by the control of the estimation winding as well as the load one during the tracing of the trajectory t_1. The estimated position $\widehat{\vartheta}_{me}^{abc}$ is used to measure the sensorless trajectory t_2, as in previous tests. Fig. 3.15 depicts the block scheme of the experiment.

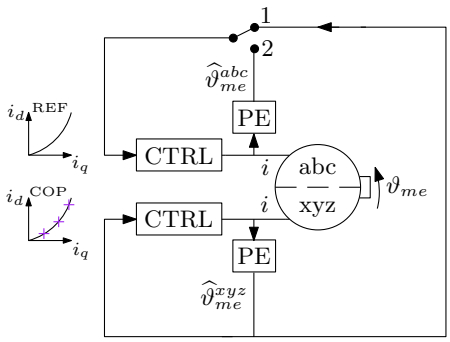

Figure 3.15: Six-phase control: part 2 block scheme of the experiment. The estimation winding is supplied and operate at constant operating points along REF. its estimated position $\widehat{\vartheta}_{me}^{xyz}$ replaces the measured one. When the switch is in position 1 the motor operates in complete sensorless mode.

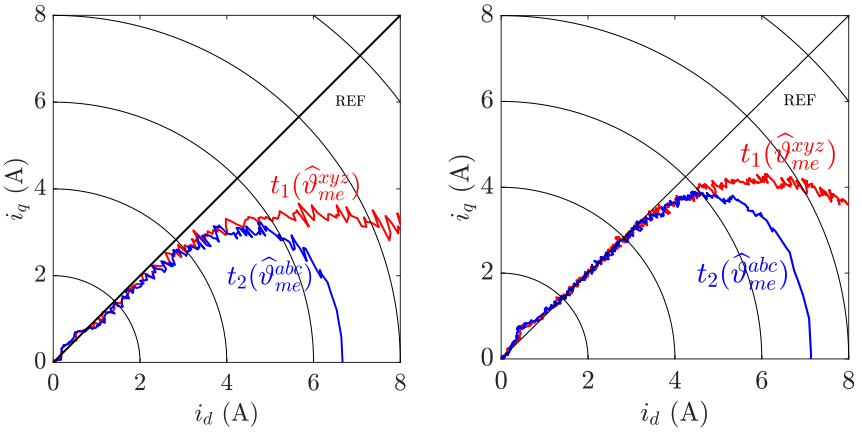

(a) $(i_d^{xyz}, i_q^{xyz}) = (1, 1)$ A, (b) $(i_d^{xyz}, i_q^{xyz}) = (3, 3)$ A,

Figure 3.16: Six-phase control: part 2. Load winding observer trajectories when $\widehat{\vartheta}_{me}^{xyz}$ from the estimation winding replaces the measured one.

Fig. 3.16 shows the experimental results obtained with the estimating three-phase system working in two different COP.

The sensorless trajectory t_2, i.e., the currents in the estimated $d^x q^x$ reference frame, is computed as follow:

$$\begin{aligned} i_d^x &= i_d \cos(\widehat{\vartheta}_{me}^{abc} - \widehat{\vartheta}_{me}^{xyz}) - i_q \sin(\widehat{\vartheta}_{me}^{abc} - \widehat{\vartheta}_{me}^{xyz}) \\ i_q^x &= i_d \sin(\widehat{\vartheta}_{me}^{abc} - \widehat{\vartheta}_{me}^{xyz}) + i_q \cos(\widehat{\vartheta}_{me}^{abc} - \widehat{\vartheta}_{me}^{xyz}) \end{aligned} \tag{3.1}$$

where the measured position is replaced by the estimated $\widehat{\vartheta}_{me}^{xyz}$. It is worth noting that these currents are not equal to the applied reference current trajectory. Indeed, the corresponding angle for the Park transformation is equal to the difference between the estimated position from the abc set and the estimated one from the xyz set, i.e., the position that substitute the measured one. It can

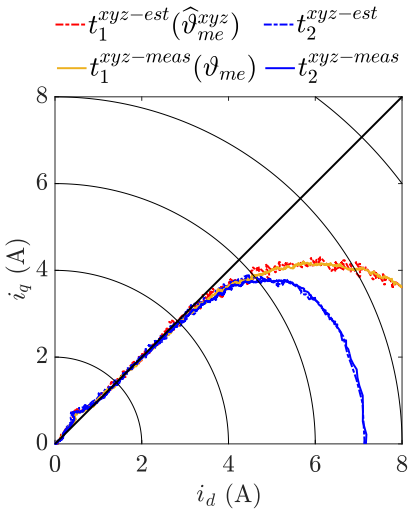

Figure 3.17: Comparison of the load winding observer trajectories when the estimation one operates at 3 A in complete sensorless and sensored mode.

be noted that the self-sensing capability of the load winding is superior when the estimation winding has a higher current, according to the analysis carried out in Section 3.3.3.

Fig. 3.17 compares the sensored and sensorless trajectories obtained by closing the estimation winding control loop either with its estimated position (complete sensorless mode) or with the measured one. It is worth remembering that when the motor is operating in complete sensorless mode, both sets are operating with the estimated position from the estimation winding during the t_1 calculation (${t_1}^{xyz-est}$ $(\widehat{\vartheta}_{me}^{xyz})$). Otherwise, when the estimation winding operates with the measured position, the tracing of the trajectory t_1 is done by using the measured position to close both windings control loops (${t_1}^{xyz-meas}$ (ϑ_{me})). As a consequence, if the sensored trajectory t_1 overlap in the two aforementioned conditions, it means that the complete sensorless control can fully substitute the sensored one without noticeable error. Which confirms the main idea and the results obtained with the investigation on the motor self-sensing capability. Measured rotor position can be replaced without self-sensing capability degradation by the estimated one obtained with a three-phase electrical system operating at low current level.

It is worth remembering that the complete sensorless mode just analysed refers to the condition where the rotor of the motor is locked. It is equivalent to the motor operating at zero or standstill condition. The estimation error between the measured position and $\widehat{\vartheta}_{me}^{xyz}$ is shown in Fig. 3.18 and it is negligible as smaller than $0.02\,\mathrm{rad}$. This is further proof of good performance of the proposed control strategy under zero or standstill conditions.

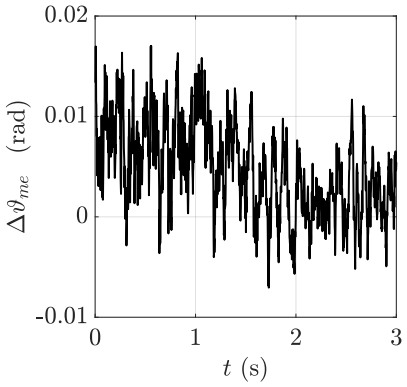

Figure 3.18: Six-phase control: part 2. Estimation error between the measured position and the estimated one from the estimation winding $\widehat{\vartheta}_{me}^{xyz}$ working at $(i_d^{xyz}, i_q^{xyz}) = (3, 3)$ A. Standstill operation in complete sensorless mode.

3.3.5 Six-Phase Control: part 3

The aim of this section is to further validate the proposed post-fault sensorless control. The motor is coupled to a PMSM motor and dragged at $50\,\mathrm{rpm}$. Both sets control loops are closed on the estimated position obtained by the estimating winding operating at low current, as in test carried out in Section 3.3.4. The load winding is controlled to follow a current reference till its nominal value. Fig. 3.19 depicts the position estimation error during the test which amplitude is comparable to the one shown in Fig. 3.18.

It is worth remembering that both test are carried out in the same conditions, except for the operating motor speed. Fig. 3.20 depicts the current trajectory of the load winding in the rotating current plane obtained by using the measured or the estimated rotor position. The current reference line is depicted, as well. For sake of comparison, both standstill and steady state condition tests are reported. It is worth remembering that the current trajectory of the load winding depicted in Fig. 3.20 does not correspond to the observer trajectory. Indeed, the process to calculate it is slightly different. Park transformation was performed to calculate the currents in the estimated $d^x q^x$ reference frame by using $\widehat{\vartheta}_{me}^{xyz}$. Same transformation is then repeated by using the measured position. Since a small estimation error occurs in the $\widehat{\vartheta}_{me}^{xyz}$, the operating point of the load winding obtained with the two transformations are different. The currents in the $d^x q^x$ reference frame depict the fictitious operating points in complete sensorless mode. Nevertheless, the actual operating points are not located along these trajectory. The real operating points are those obtained by using the measured position to compute the reference frame transformation. Fictitious and real operating points overlap with the reference for low current values. A slightly oscillation is depicted when the

machine saturates. As mentioned, the process of calculation is different from the one to calculate the observer trajectories as in (3.1).

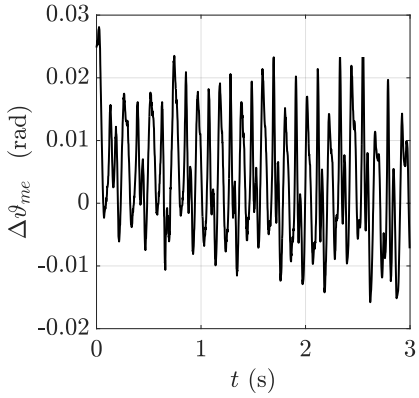

Figure 3.19: Six-phase control: part 3. Estimation error between the measured position and $\widehat{\vartheta}_{me}^{xyz}$ from the estimation winding working at $(i_d^{xyz}, i_q^{xyz}) = (3, 3)$ A. Complete sensorless operation when the motor rotates at $50\,\mathrm{rpm}$.

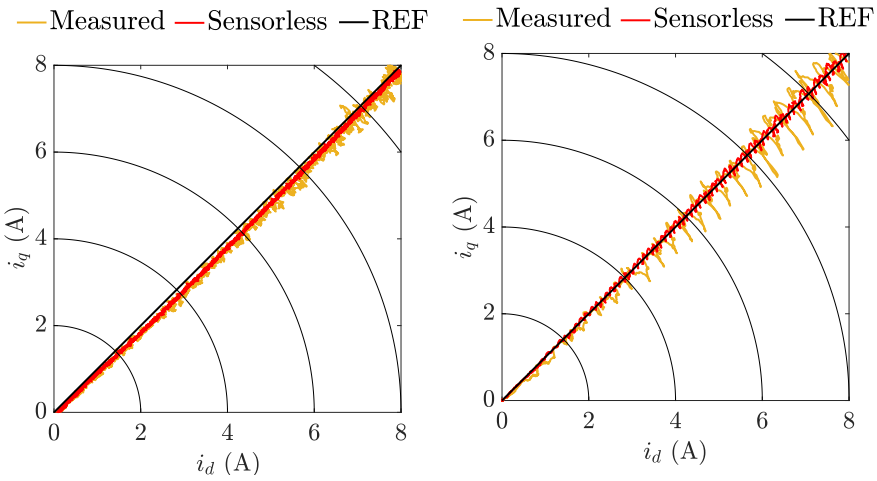

(a) Standstill condition,

(b) Steady state condition,

Figure 3.20: Six-phase control part 3. Load winding current in the rotating reference frame obtained both with the measured and estimated rotor position. Both standstill and steady state at $50\,\mathrm{rpm}$ tests are reported.

The load winding exhibits a stable behaviour since current follows the desired reference. It is worth noting that a 40% overload current is applied in both tests without any stability issue. In such condition the motor is expecting to produce almost 70% of the rated nominal torque from FEA simulation analysis. The estimating winding provided a reliable and error-free rotor

position estimation since it works at low current values where the cross-coupling effect is negligible. In turn, the load winding is able to work in the desired working condition even in overload.

Finally, it is worth noting that the sensorless trajectory t_2 diverged around $5\,\mathrm{A}$ in the HC test (see Section 3.3.2) where the load winding is closed on the estimated position obtained by its estimator (the xyz electrical system is disconnected) whereas the proposed scheme exhibits a stable behaviour over the whole current range.

3.4 Conclusion

A post-fault sensorless control strategy based on the study of the self-sensing capability of a dual three-phase synchronous reluctance motor is investigated. Different supply scenarios, namely, three-phase and half-control conditions, has been analysed, and FEA analysis and experimental results are compared. In both configurations, the motor is not able to operate in sensorless mode at full load since the system in unstable due to the large estimation error induced by the cross-saturation inductance. The peculiar self-sensing capability and the additional degree of freedom of a DT motor are exploited by the proposed low-speed sensorless strategy. The former three-phase electrical winding operates at low speed and estimates the rotor position by injecting a HF rotating signal in the stator reference frame. The ellipse fitting estimation algorithm is exploited to retrieve the rotor position since no motor parameters knowledge are required for its design and tuning. The negligible magnetic saturation at low load condition allows an error-free rotor position estimation which is used by both three-phase electric drives. The latter electric system can operate and accurately follow its current reference, even in overload condition. An extended experimental campaign proved the proposed control strategy. The proposed sensorless algorithm allows controlling a dual-three synchronous reluctance motor in mechanical sensor post-fault condition. No motor parameters are required for the estimation of the rotor position as well as compensation algorithm. The motor performance is reduced as a three-phase system must work at low current level but the service continuity is guaranteed and the motor is able to exploit up to 70% of the nominal torque in the analysed condition.

4 KALMAN FUSION FEASIBILITY STUDY FOR SENSORLESS CONTROL OF A MULTIPHASE MACHINE

This chapter investigates the feasibility and the performance of sensor fusion techniques in a sensorless drive in the case of a fault in the position sensor. The same motor as the one used in Section 3, as well as the decomposition method using the MS approach. Since the motor is studied as two three-phase sets, it is possible to implement two position estimators, one for each winding.

As a consequence, two estimated positions are available in the overall control scheme as shown in Fig. 4.1. The idea of this chapter is to fuse the two estimated positions to obtain an unique variable to close both control loops. The Closed Loop (CL) block contains the control algorithm for each three-phase winding. It is made up of the current control loop, the HF injection in the stationary $\alpha\beta$ reference frame and a LPF to extract the low frequency components of the measured currents to close the current loop. No complex compensation methods are used to perform sensorless control and as a result the motor is able to operate sensorless with good performance. The two estimated positions $\widehat{\vartheta}_{me}^{abc}$ and $\widehat{\vartheta}_{me}^{xyz}$ are merged with the implemented fusion algorithm and both control loops are closed on the fused state $\widehat{\vartheta}_{me}^{x}$. The superscript is needed because two different fusion approaches are evaluated. The former one is a non-weighted average, the two estimated positions are fused by applying same weight to them. The second one is a Kalman filter sensor fusion implementation. KF sensor fusion is used to properly weight the two estimated positions as will be explained in Section 4.1.2. Hence, the superscript will refers to the considered winding set or fused variable.

The control strategy of the machine is the same implemented in Section 3. The two three-phase sets are controlled at different operating points, hence the two estimated positions will have different accuracy depending on the operating point of the three-phase set. To use both estimated positions to control the machine, a proper strategy to mix the estimated variables needs to be found.

The performance of the two approaches are compared through the online calculation of the OL position error. The open loop position error $\Delta\vartheta_{me}^{x}$ is defined as the difference between the measured position and the estimated one. The algorithms are developed for the same motor used in Section 3.1, as well as the motor modelling strategy using the MS approach. Different supply scenarios are evaluated, an extensive experimental stage is performed to find the most suitable sensor fusion strategy to apply in the case of a fault in the position sensor for a multiphase machine.

The chapter is organized as follows. The adopted measurement fusion techniques are thoroughly described in Section 4.1. The results are illustrated

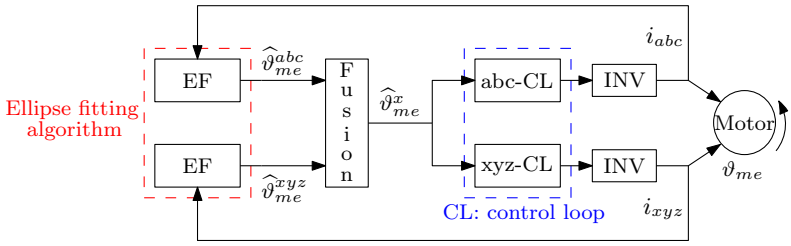

Figure 4.1: Adopted control scheme of the proposed sensor fusion algorithm: the estimated positions of the two windings are fused together to obtain an unique estimation to close both control loops.

in Section 4.2. Particularly in Section 4.2.1, a deep discussion and comparison about the two implemented fusion algorithms is done. Then in Section 4.2.2, sensorless control is performed with the chosen technique. Finally, Section 4.3 exhibits the conclusion.

4.1 Measurement Fusion Techniques

The purpose of the fusion technique is to have an unique fused state that closes both control loops. Two different techniques are used to merge together the two estimated positions from the two winding sets. The former one is a non-weighted average, whereas the latter refers to the Kalman fusion algorithm implementation.

4.1.1 Non-Weighted Mean Average

The non-weighted mean average merges the two estimated positions to obtain the estimated mean average position $\widehat{\vartheta}_{me}^{mean}$ as follows:

$$\widehat{\vartheta}_{me}^{mean} = \frac{\widehat{\vartheta}_{me}^{abc} + \widehat{\vartheta}_{me}^{xyz}}{2}. \tag{4.1}$$

It is worth remembering that the estimation error is a function of the operating point. Hence, if the two three-phase windings operate at different operating points, ϵ will be different. With (4.1) the output of the algorithm is not properly weighted in the aforementioned operating condition. Nevertheless, the algorithm has low computational cost. The performance of the estimated $\widehat{\vartheta}_{me}^{mean}$ are evaluated by means of the average position error $\Delta\vartheta_{me}^{mean}$ calculated as:

$$\Delta\vartheta_{me}^{mean} = \vartheta_{me} - \widehat{\vartheta}_{me}^{mean}. \tag{4.2}$$

4.1.2 Kalman Filter Algorithm

Kalman filter is one of the most popular algorithm based on a state-space representation of the model. It is employed to approximate the state of a

Table 4.1: Kalman filter algorithm variables and size.

Symbol	Quantity	Size
$\mathbf{x}$	State vector	$n_x \times 1$
$\mathbf{A}$	State matrix	$n_x \times n_x$
$\mathbf{B}$	Input matrix	$n_x \times n_u$
$\mathbf{u}$	Input vector	$n_u \times 1$
$\mathbf{y}$	Output vector	$n_y \times 1$
$\mathbf{C}$	Observation matrix	$n_y \times n_x$
$\mathbf{w}$	Process noise vector	$n_x \times 1$
$\mathbf{v}$	Measurement noise vector	$n_y \times 1$
$\mathbf{P}$	State covariance matrix	$n_x \times n_x$
$\mathbf{Q}$	Process noise covariance matrix	$n_x \times n_x$
$\mathbf{R}$	Measurement noise covariance matrix	$n_y \times n_y$
$\mathbf{G}$	Kalman gain	$n_x \times n_y$

process through recursive equations, which provide minimum error. The KF is based on the assumption that the true state at time k is evolved from the state at time $k-1$. Furthermore, at time k a measurement of the true state is available as follows:

$$\begin{aligned} \mathbf{x_k} &= \mathbf{A x_{k-1}} + \mathbf{B u_k} + \mathbf{w_k} \\ \mathbf{y_k} &= \mathbf{C x_k} + \mathbf{v_k} \end{aligned} \tag{4.3}$$

where the variables definition and their size are listed in Tab. 4.1. The bold symbols refer to variables that are vectors or matrices. The size of a quantity is indicated with the symbol n and a subscript referring the relative variable.

The process noise matrix $\mathbf{w}$ accounts for disturbances and model inaccuracies, while $\mathbf{v}$ represents the measurement noise. The noises are assumed to be white Gaussian noises with covariance matrices $\mathbf{Q}$ and $\mathbf{R}$ referring to the process and measurement noise, respectively. The covariance matrices are symmetric, positive semi-definite and independent from the state.

Kalman filter is a recursive estimator method where the state at epoch k is computed from the previous state at epoch $k-1$. The algorithm involves two distinct stages, whose equations are given below.

Prediction:
calculate the predicted state $\hat{\mathbf{x}}_\mathbf{k}$ and the state covariance matrix $\mathbf{P_k}$ at epoch k based on the epoch $k-1$:

$$\begin{aligned}\widehat{\mathbf{x}}_{\mathbf{k|k-1}} &= \mathbf{A}\widehat{\mathbf{x}}_{\mathbf{k-1|k-1}} + \mathbf{B}\mathbf{u}_{\mathbf{k}} \\ \mathbf{P}_{\mathbf{k|k-1}} &= \mathbf{A}\mathbf{P}_{\mathbf{k-1|k-1}}\mathbf{A}^{\mathbf{T}} + \mathbf{Q}_{\mathbf{k}}.\end{aligned} \tag{4.4}$$

Correction:
update the predicted state $\widehat{\mathbf{x}}_{\mathbf{k}}$ with the new information at time k through the Kalman gain $\mathbf{G}_{\mathbf{k}}$ calculation:

$$\begin{aligned}\mathbf{G}_{\mathbf{k}} &= \mathbf{P}_{\mathbf{k|k-1}}\mathbf{C}^{\mathbf{T}}(\mathbf{C}\mathbf{P}_{\mathbf{k|k-1}}\mathbf{C}^{\mathbf{T}} + \mathbf{R}_{\mathbf{k}})^{-1} \\ \mathbf{P}_{\mathbf{k|k}} &= (\mathbf{I} - \mathbf{G}_{\mathbf{k}}\mathbf{C})\mathbf{P}_{\mathbf{k|k-1}} \\ \widehat{\mathbf{x}}_{\mathbf{k|k}} &= \widehat{\mathbf{x}}_{\mathbf{k|k-1}} + \mathbf{G}_{\mathbf{k}}(\mathbf{y}_{\mathbf{k}} - \mathbf{C}\widehat{\mathbf{x}}_{\mathbf{k|k-1}})\end{aligned} \tag{4.5}$$

where $\mathbf{I}$ is the identity matrix. It can be demonstrated that a minimization of the residual error to find the optimal Kalman gain is obtained.

Kalman fusion method implemented in this dissertation merges the sensor data incrementing the size of the output vector $\mathbf{y}$. Therefore, $\mathbf{y}$ is a column vector with the number of rows equal to the sensors used. Two variables are measured, i.e. the two estimated positions. Hence $\mathbf{y}$ is a column vector with two rows and one column. The state to be known is the Kalman fusion estimated position $\widehat{\vartheta}^{k}_{me}$, so it is a vector with size $[1 \times 1]$. The size of the observation matrix needs to be chosen accordingly. The observation matrix $\mathbf{C}$ maps the state vector into the output vector, hence it indicates which state variables are included into the output and which are not. Since the implemented algorithm merges together the sensor data, the covariance matrix $\mathbf{R}$ is the merge of the covariance matrices of the sensors used. It is a diagonal matrix where the non-zero elements are the covariance matrices for each sensor, i.e. the sensor's variance itself. For more clarity, all dimensions of the matrices are listed below.

$$\begin{aligned}\mathbf{y} &= [\widehat{\vartheta}^{abc}_{me} \;\; \widehat{\vartheta}^{xyz}_{me}]^T \\ \mathbf{x} &= [\widehat{\vartheta}^{k}_{me}] \\ \mathbf{A} &= [1] \\ \mathbf{B} &= [0] \\ \mathbf{C} &= [1\;1]^T \\ \mathbf{Q} &= [0.1] \\ \mathbf{R} &= \begin{bmatrix} E(\widehat{\vartheta}^{abc}_{me}) & 0 \\ 0 & E(\widehat{\vartheta}^{xyz}_{me}) \end{bmatrix}\end{aligned} \tag{4.6}$$

where no knowledge about the model is assumed, hence $\widehat{\mathbf{x}}_{\mathbf{k|k-1}} = \widehat{\mathbf{x}}_{\mathbf{k|k}}$.

The value of the matrix $\mathbf{R}$ is determined offline by measuring the estimated positions and then calculating their variance. The process noise covariance

Table 4.2: Summary of the experimental tests: scenarios and key results

Test	Scenario	abc set operating point	xyz set operating point	Key results
1	1	3 A	3 A	Kalman fusion and mean-average have the same performance
	2	1 A	4 A	Kalman filter weights correctly the two estimated positions → chosen fusion algorithm
	3	ramp reference	1 A	Test with the adopted control strategy in open loop
2	//	ramp reference	1 A	Test in complete sensorless mode → No sensorless control divergence and good performance achieved

matrix value is determined experimentally by evaluating the performance of the algorithm. The correctness of $\widehat{\vartheta}^k_{me}$, is determined through the online calculation of the Kalman filter position error as follows:

$$\Delta\vartheta^k_{me} = \vartheta_{me} - \widehat{\vartheta}^k_{me}. \tag{4.7}$$

4.2 Results

An extensive experimental stage is performed to study the feasibility and performance of sensor fusion strategy. The MUT parameters as well as the injection quantities are listed in Section 3.3 in Tab. 3.3 and Tab. 3.4, respectively. The test bench is the same as the one showed in Fig. 3.7. A detail of the adopted motor is shown in Fig. 4.2. It is possible to see the terminal block from which the windings arrangement of the machine can be changed. Sensorless control strategy implemented in this analysis has been discussed in Section 2.2.1.

Two different tests are carried out to prove the effectiveness of the measurement fusion. In the former the motor is controlled sensored. Both the non-weighted average and KF fusion algorithms are implemented and the

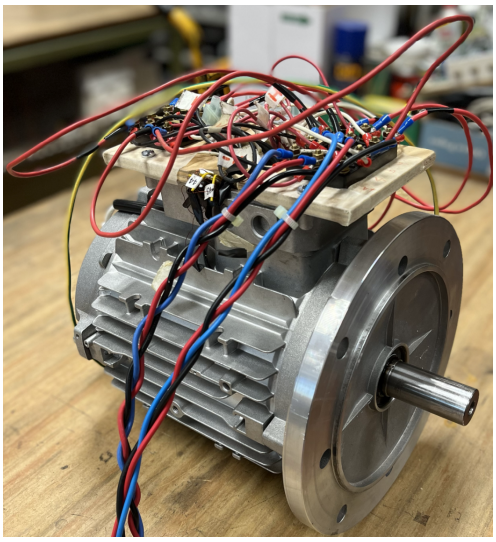

Figure 4.2: Detail of the adopted motor.

position errors are calculated with (4.2) and (4.7). Furthermore the coefficients of the measurement noise covariance matrix are retrieved by measuring the variance of the estimated positions $\widehat{\vartheta}_{me}^{abc}$ and $\widehat{\vartheta}_{me}^{xyz}$. The test is reported in Section 4.2.1. The second test is aimed to perform the complete sensorless control. Both control loops are closed on the Kalman fusion state $\widehat{\vartheta}_{me}^{k}$ simulating a fault in the position sensor and the performance of the algorithm are evaluated in closed loop. The test is described in Section 4.2.2.

For more clarity, Tab. 4.2, summarizes the main condition of the tests.

4.2.1 Evaluation of the Fusion Algorithms in Open Loop for Different Supply Scenarios

In this test the two three-phase windings are controlled in different operating points. Several supply scenario in which the two sets are controlled at different operating points and conditions are evaluated. The goal is to find the more suitable fusion algorithm between the aforementioned mean-average and Kalman fusion. It is worth remembering that all the tests are experimental. The measured position is used to close both CL in the first stage to avoid sensorless control divergence before using and tuning the algorithms. Kalman filter one, especially. The performance of the two fusion techniques are therefore compared in open loop through the calculation of the position errors. Three different supply scenarios are analyzed.

In the first supply scenario, the two three-phase sets are controlled at the same operating point: $|I| = 3$ A. Fig. 4.3a shows the estimation errors of the two sets whereas Fig. 4.3b shows the comparison between the non-weighted mean average position error $\Delta\vartheta_{me}^{mean}$ and the KF one $\Delta\vartheta_{me}^{k}$. Same perfor-

Table 4.3: Variance of the estimated variables when the two windings operate at the same operating points $|I| = 3$ A.

$E(\widehat{\vartheta}_{me}^{abc})$	$E(\widehat{\vartheta}_{me}^{xyz})$	$E(\widehat{\vartheta}_{me}^{k})$	$E(\widehat{\vartheta}_{me}^{mean})$
$4.9586 \cdot 10^{-4}$	$4.9586 \cdot 10^{-4}$	$3.4265 \cdot 10^{-4}$	$3.4265 \cdot 10^{-4}$

mance of the two fusion algorithms are reached in this operating condition. Indeed, the inputs, i.e., the two estimated positions, are equals. For this test and for the followings, the variance of the estimated position is calculated to analyze better the performance of the investigated algorithms. Tab. 4.3 shows the variance for the analyzed operating condition. As expected, since the operating point is the same $E(\widehat{\vartheta}_{me}^{abc}) = E(\widehat{\vartheta}_{me}^{xyz})$ and $E(\widehat{\vartheta}_{me}^{mean}) = E(\widehat{\vartheta}_{me}^{k})$.

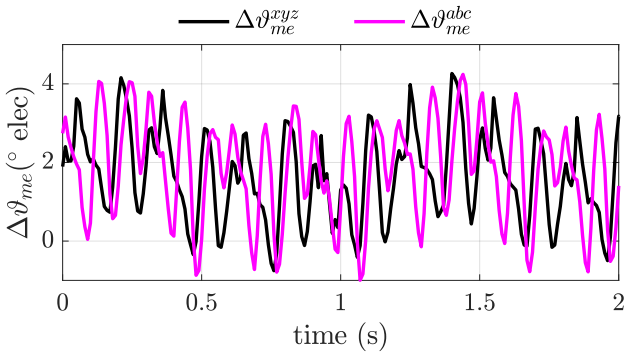

(a) abc and xyz windings estimation errors,

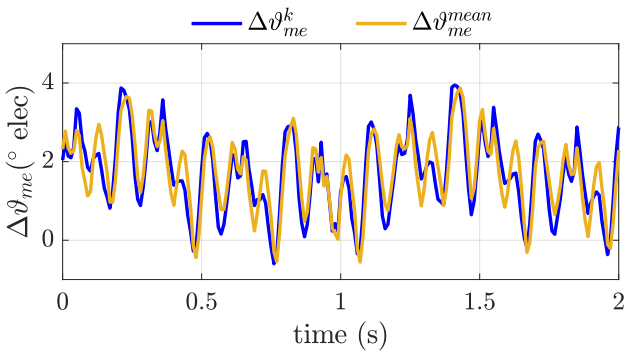

(b) Kalman fusion and mean average estimation errors,

Figure 4.3: Position errors calculated when the two three-phase windings operate at the same operating point $|I| = 3$ A.

Different current references are applied to the two three-phase sets in the second scenario. The operating points are $(i_d^{abc}, i_q^{abc}) = (1, 1)$ A and $(i_d^{xyz}, i_q^{xyz}) = (4, 4)$ A, for the abc and xyz winding, respectively. Fig. 4.4a shows the estimation errors of the two three phase sets. It is worth remembering that, as deeply discussed in Section 2.2.2, the estimation error is a function of the operating

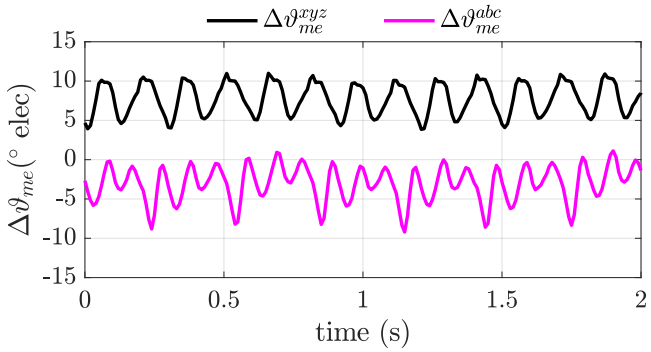

(a) abc and xyz windings estimation errors,

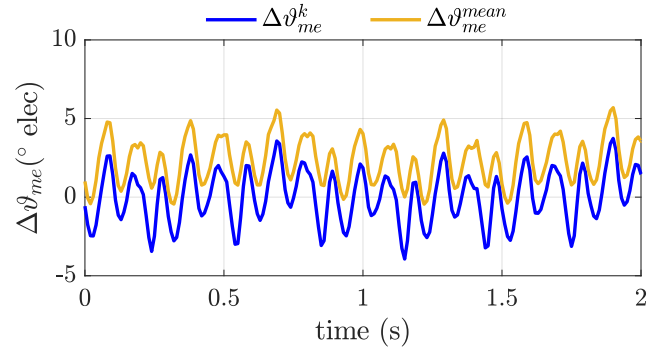

(b) Kalman fusion and mean average estimation errors,

Figure 4.4: Position errors calculated when the two three-phase windings operate at $(i_d^{abc}, i_q^{abc}) = (1, 1)$ A and $(i_d^{xyz}, i_q^{xyz}) = (4, 4)$ A.

point of the machine. As a consequence, in this scenario two different position errors are expected since the two sets operate at different operating points. The difference is due to the cross-inductance terms that change with the current amplitude, accordingly the position error. The $\Delta\vartheta_{me}^{abc}$ is slightly lower than $\Delta\vartheta_{me}^{xyz}$ since a lower current reference is applied to the abc winding compared to the xyz one. The performance of the Kalman fusion algorithm and the non-weighted average are different as shown in Fig. 4.4b. The former one is able to properly weight the two estimated positions and the bias error is almost eliminated whereas the latter one apply the same weight to the estimated positions. Tab. 4.4 shows the calculation of the variance for all the estimated variables. It is worth noting that the variance of $\widehat{\vartheta}_{me}^{k}$ is slightly lower than the average one.

A ramp-wise reference is applied to the abc winding whereas the xyz one is controlled at $(i_d^{xyz}, i_q^{xyz}) = (1, 1)$ A in the third scenario. The results of the test are shown in Fig. 4.5. The position error of the xyz winding is almost constant since it operates at the same operating point for the whole test. A ramp-wise current reference is applied to the abc winding, hence a ramp-wise pattern is highlighted in $\Delta\vartheta_{me}^{abc}$. By computing the non-weighted average and

Table 4.4: Variance of the estimated variables when the two three-phase windings operate at $(i_d^{abc}, i_q^{abc}) = (1, 1)$ A and $(i_d^{xyz}, i_q^{xyz}) = (4, 4)$ A.

$E(\widehat{\vartheta}_{me}^{abc})$	$E(\widehat{\vartheta}_{me}^{xyz})$	$E(\widehat{\vartheta}_{me}^{k})$	$E(\widehat{\vartheta}_{me}^{mean})$
0.0016	0.0013	$7.7655 \cdot 10^{-4}$	$8.7802 \cdot 10^{-4}$

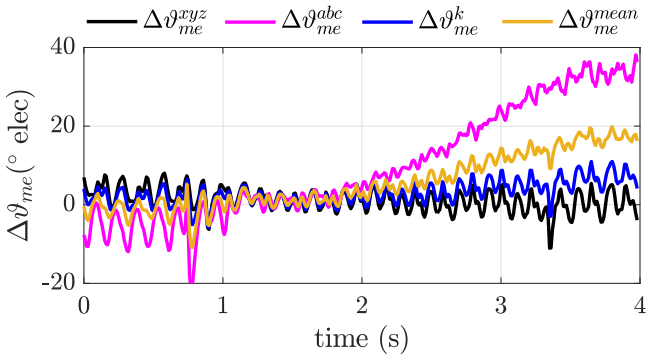

Figure 4.5: Three-phase windings, Kalman fusion and non-weighted average position errors calculated when the xyz winding operates at $(i_d^{xyz}, i_q^{xyz}) = (1, 1)$ A and a ramp-wise reference is applied to the abc one.

the Kalman filter algorithm one, the two position errors are calculated online. A noticeable difference appears between $\Delta\vartheta_{me}^{mean}$ and $\Delta\vartheta_{me}^{k}$. Same weight is applied to both estimated variables from the the former approach. As a result, the position error of the abc winding that follows a ramp-wise pattern, has the same weight compared to the xyz one that is operating at constant low current. It is worth remembering that the position error is a function of the operating point, hence the estimated position from the xyz winding is more truthful than the abc one and it is incorrect to assign the same weight for both estimated variables.

In addition sensorless control using $\widehat{\vartheta}_{me}^{mean}$ it is not possible because $\Delta\vartheta_{me}^{mean}$ is about $20°$ elec when the abc winding is operating at its rated current. Sensorless control divergence and stability issues can arise. Kalman filter is able to properly weight the two estimated positions and $\Delta\vartheta_{me}^{k}$ is almost zero.

The control strategy used in the last scenario will be adopted during the sensorless control in Section 4.2.2 simulating a fault in the position sensor. To control the motor without position sensor and complex compensation methods, the estimated positions from the two winding sets will be fused together to have an unique variable to close both control loops. Accordingly, it is not possible to use the non-weighted average and the Kalman fusion algorithm is chosen.

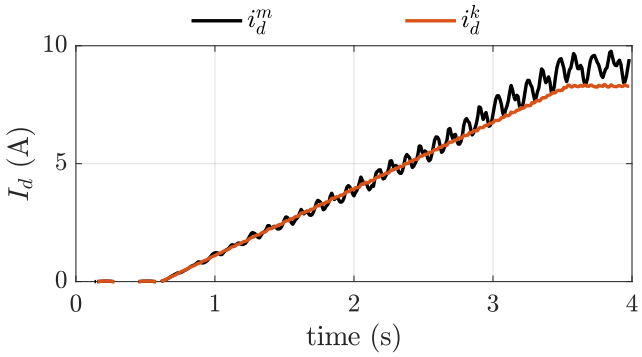

(a) d-axis currents,

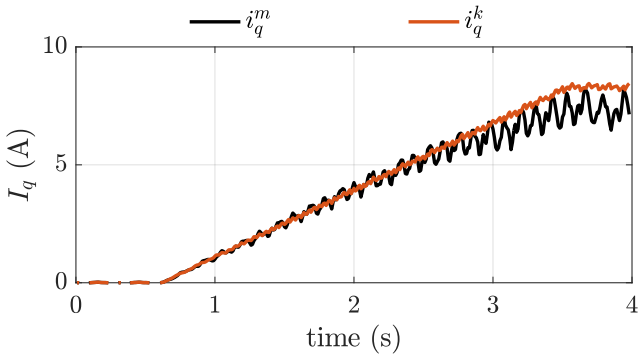

(b) q-axis currents,

Figure 4.6: abc winding currents transformed using the measured position (i_d^m,i_q^m) and the fused one (i_d^k,i_q^k) when both control loops are closed on the fused state $\widehat{\vartheta}_{me}^k$. The motor is operating sensorless.

4.2.2 Kalman Fusion Performance in Closed Loop

In this test, both control loops are closed on the fused position from the Kalman fusion algorithm and the motor is controlled sensorless. The measured position is acquired only to evaluate the performance of the developed algorithm. The MUT is coupled to a PMSM and dragged at $50\,\mathrm{rpm}$. The Kalman fusion estimated state $\widehat{\vartheta}_{me}^k$ is a properly weighted variable, so according to the values of the measurement noise covariance matrix $\mathbf{R}$, one measure may have more relevance than another, and thus it is more truthful. In this experiment the xyz winding operates at constant current whereas the abc one follows a ramp-wise reference. According to the previous test, the former estimated position has greater relevance than the latter one. Fig. 4.6 shows the abc winding currents transformed in the dq reference frame by means of the measured position (i_d^m,i_q^m) and then in the estimated $d^x q^x$ reference frame by means of the fused one (i_d^k,i_q^k). The latter one are the fictitious operating points in sensorless mode. Nevertheless the real operating points (i_d^m,i_q^m) are those obtained by using the measured position.

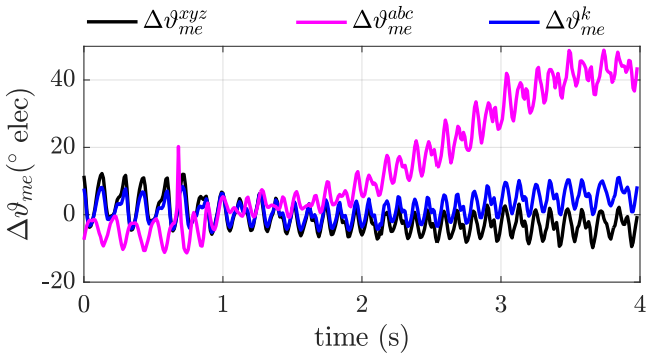

Figure 4.7: Position errors of the two windings and Kalman fusion position error when both control loops are closed on the fused state and sensorless control is performed.

A slightly difference appears between (i_d^m,i_q^m) and (i_d^k,i_q^k) due to a small position error $\Delta\vartheta_{me}^k$. The $\Delta\vartheta_{me}^k$, as well as the position errors of the two sets, is shown in Fig. 4.7. The fused position error is a weighted output of the Kalman fusion algorithm, during the first part of the test is basically zero since both the abc and xyz winding currents are low. Then it increments its value since the abc current grows and, in turns, its position error. At the end of the test its value it is about $5°$ elec. Explaining the little deviation between (i_d^m,i_q^m) and (i_d^k,i_q^k). It is worth remembering that the motor is operating sensorless with both control loops closed on $\widehat{\vartheta}_{me}^k$.

4.3 Conclusion

An investigation on the feasibility of the Kalman fusion algorithm is proposed for a dual three-phase synchronous reluctance machine. The developed control strategy is verified through an extensive experimental stage and the motor is tested under different supply scenarios. Each three-phase winding is supplied by a dedicated inverter and a position estimation algorithm is applied for each set resulting into two different estimated positions. The two estimated variables are fused together by means of a non-weighted average and the Kalman fusion algorithm. The performance of the two methods are compared by supplying the motor under different scenarios.

In the first test, the open loop position error is calculated for both three-phase windings and the two fusion ones. Kalman filter sensor fusion estimated position perfectly fits the chosen control algorithm because it is able to properly weight the reference variables. The two three-phase windings are controlled in different operating points to provide a fault tolerant sensorless control strategy in case of a fault in the position sensor by using both estimated positions. In the latter test, both control loops are closed on the fused position from the Kalman fusion algorithm and the performance are evaluated. The motor is

able to operate sensorless with the merged position showing good sensorless performance in the case of a fault in the position sensor.

5 Modelling of a Rotating Signal Injection-Based Position Observer for Sensorless Synchronous Electric Drives

Model-based design methods are used to reach optimal performance of an electric drive. However, these methods require an accurate plant model that must be provided. Current and speed control loops interact together with the observer regulator in a sensorless drive. Hence, a correct description of the system is mandatory to reach optimal performance of the electric drive. Stability issue and inaccuracy of the estimated position are the main flaws of an inaccurate model. Co-sinusoidal functions are used together with filters in the modulation/demodulation process to retrieve the estimated position in low speed or standstill sensorless control. Therefore, both time and Laplace domain variables are used in the system plant.

Conventional approach mix together time and Laplace variables to retrieve the position observer TF. This leads to an inaccuracy in the description of the plant since the demodulation effects on the filters TFs are not considered. A new formulation of the observer TF for rotating injection-based techniques is proposed in this chapter. The modulation/demodulation theory is exploited to derive the estimator TF completely in the Laplace-domain. The accuracy of the proposed TF is verified with several regulators designed with two approaches, namely, DS and IMP. Theoretical considerations and accuracy of the proposed model are verified through an extensive simulation stage. Time response and position tracking of different regulators designed for a wide range of bandwidth are investigated. Finally, the performance of the regulators designed with the conventional observer TF and the proposed one are compared highlighting the flaws of the former approach.

The position observer is modeled for a three-phase PMSM. Rotating voltage signal injection theory has been reported in Section 2.2. A more specific system representation for rotating signal injection is shown in Fig. 5.1. The electrical motor dynamic functions are expressed as $G_d(s)$ and $G_q(s)$. The measured stator currents in the $\alpha\beta$ reference frame are filtered by means of an high pass filter to isolate the HF components. For more simplicity, as in this chapter Laplace domain variables are exploited, the filters TF will be cited as $F_{\mathrm{HPF}}(s)$ and $F_{\mathrm{LPF}}(s)$, for the high pass and low pass filter, respectively. As shown in (2.10), the estimated rotor position can be retrieved from the negative sequence through modulation/demodulation process in the demodulator block. Sine and cosine functions that depend both on ω_h and on the estimated rotor position $\widehat{\vartheta}_{me}$, are multiplied by the HF currents and the signals are added together. The demodulation process adds an oscillating components at twice the injected frequency that is eliminated by filtering the signal z_1 with a

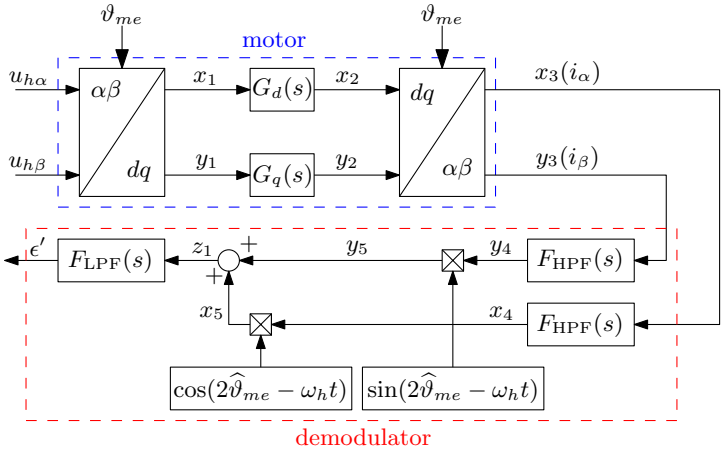

Figure 5.1: Rotating voltage injection system representation.

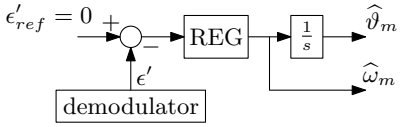

Figure 5.2: Position observer scheme.

low-pass filter $F_{\mathrm{LPF}}(s)$ to find the error signal ϵ'.

The cross-inductance term introduces an error ϵ as highlighted in (2.19), nevertheless the dynamic of the observer is not affected by the l_{dq} effect. Accordingly, the contribution of the l_{dq} is neglected from now on. The demodulated error signal ϵ' is obtained as:

$$\epsilon' = \frac{U_h l_\Delta}{\omega_h l_{dd} l_{qq}} \sin(2(\vartheta_{me} - \widehat{\vartheta}_{me})) \approx \frac{2U_h l_\Delta}{\omega_h l_{dd} l_{qq}} (\vartheta_{me} - \widehat{\vartheta}_{me}) \tag{5.1}$$

where a small estimation error is assumed to approximate the sine function with its argument. The difference between the measured position and the estimated one is defined as the position error $\Delta\vartheta_{me} = \vartheta_{me} - \widehat{\vartheta}_{me}$. Finally, the error signal is driven to zero by means of a REG to obtain the estimated electromechanical speed $\widehat{\omega}_m$ and with the use of an integrator, the estimated electrical position as shown in Fig. 5.2. It is worth noting that the design of the regulator strictly depends on the plant model. An inaccurate observer description lead to a wrong regulator tuning, hence the dynamic performance of the electric drive is affected.

This chapter is organized as follows. The proposed estimator TF is thoroughly explained in Section 5.1. The observer regulator design by means of two different methods is described in Section 5.2. Simulation results to show the accuracy of the proposed model are reported in Section 5.3. Finally, the conclusion are reported in Section 5.4.

5.1 Estimator Transfer Function Analysis

5.1.1 Conventional Observer Model

Observer transfer function for rotating injection based sensorless schemes is usually derived as follows. The gain between the estimated position and the error signal obtained in (5.1), is combined with the TFs of the implemented filters in the demodulation scheme in Fig. 5.1. Hence, the conventional observer TF is:

$$P_{\text{obs}}^{\text{old}}(\text{s}) = \frac{\epsilon'(s)}{\widehat{\vartheta}_{me}(s)} = \frac{2U_h l_\Delta}{\omega_h l_{dd} l_{qq}} F_{\text{LPF}}(s) F_{\text{HPF}}(s). \tag{5.2}$$

This approach blends together time and Laplace domain variables to derive the observer transfer function. The TF gain is obtained in time domain by exploiting trigonometric functions and filters TFs are added only a posteriori. Therefore, the resulting TF in (5.2) loses the effects of demodulation on filters TFs. The aforementioned inaccuracy on the observer modelling has an impact on the regulator design and, in turns, stability issues could arise. Model-based design methods are not able to guarantee the performance of the drive if a proper plant model is not given. This lead to a wrong stability analysis and an inaccurate bandwidth, both critical points in a sensorless electric drive control. The difference between the conventional observer model and the proposed one will be shown in Section 5.1.2.

5.1.2 Proposed Observer Model

The whole rotating injection based sensorless scheme can be represented in Fig. 5.1. It is worth noting that the system is characterised by several multiplications both in motor system, namely, the Park's transformation, and in the demodulator block. These elements play a crucial role for a proper design of the observer TF, hence they represent the main element of the proposed analysis. The TF of a modulated/demodulated signal is derived in [63]. The Laplace transform of a generic modulated signal $\zeta(t) = \cos(\omega_x + \phi)x(t)$ is:

$$\mathcal{L}(\zeta) = \frac{[e^{j\phi}X(s - j\omega_x) + e^{-j\phi}X(s + j\omega_x)]}{2} \tag{5.3}$$

where $\mathcal{L}$ is the Laplace operator and $X(s)$ is the Laplace transform of the signal $x(t)$, ω_x and ϕ are a generic pulsation frequency and an arbitrary phase shift, respectively. Rotating injection sensorless scheme can be derived in the Laplace domain with any other combination of modulated and demodulated carriers by applying (5.3).

The following analysis refers to the signals in Fig. 5.1. By defining $\vartheta_{me} = \omega_{me}t$ and $\widehat{\vartheta}_{me} = \widehat{\omega}_{me}t$, it follows that the Laplace transform of signals $x_2(t)$

and $y_2(t)$ is:

$$\begin{aligned} X_2(s) = \frac{G_\Sigma(s)+G_\Delta(s)}{4}[&U_\alpha(s-j\omega_{me}) + U_\alpha(s+j\omega_{me}) \dots \\ &- jU_\beta(s-j\omega_{me}) + jU_\beta(s+j\omega_{me})], \\ Y_2(s) = \frac{G_\Sigma(s)-G_\Delta(s)}{4}[&U_\beta(s-j\omega_{me}) + U_\beta(s+j\omega_{me}) \dots \\ &+ jU_\alpha(s-j\omega_{me}) - jU_\alpha(s+j\omega_{me})] \end{aligned} \tag{5.4}$$

and that of signals $x_4(t)$ and $y_4(t)$ is:

$$\begin{aligned} X_4(s) = \frac{F_{\mathrm{HPF}}(s)}{4}\{&[U_\alpha(s)(G_\Sigma(s-j\omega_{me}) + G_\Sigma(s+j\omega_{me})) \dots \\ &+ U_\alpha(s-2j\omega_{me})G_\Delta(s-j\omega_{me}) + U_\alpha(s+2j\omega_{me})G_\Delta(s+j\omega_{me})] \dots \\ &+ j[U_b(s)(G_\Sigma(s-j\omega_{me}) - G_\Sigma(s+j\omega_{me})) \dots \\ &- U_\beta(s-2j\omega_{me})G_\Delta(s-j\omega_{me}) + U_\beta(s+2j\omega_{me})G_\Delta(s+j\omega_{me})]\}, \\ Y_4(s) = \frac{F_{\mathrm{HPF}}(s)}{4}\{&[U_\beta(s)(G_\Sigma(s-j\omega_{me}) + G_\Sigma(s+j\omega_{me})) \dots \\ &- U_\beta(s-2j\omega_{me})G_\Delta(s-j\omega_{me}) - U_\beta(s+2j\omega_{me})G_\Delta(s+j\omega_{me})] \dots \\ &+ j[U_a(s)(-G_\Sigma(s-j\omega_{me}) + G_\Sigma(s+j\omega_{me})) \dots \\ &- U_\alpha(s-2j\omega_{me})G_\Delta(s-j\omega_{me}) + U_\alpha(s+2j\omega_{me})G_\Delta(s+j\omega_{me})]\} \end{aligned} \tag{5.5}$$

where $G_\Sigma(s) = G_d(s) + G_q(s)$, $G_\Delta(s) = G_d(s) - G_q(s)$ and $U_\alpha(s)$ and $U_\beta(s)$ are the Laplace transforms of the HF injected signals in the stationary reference frame $u_\alpha(t)$ and $u_\beta(t)$, respectively. In the rotating signal injection both the signals in (5.5) have to be demodulated. The demodulated signals can be written as $X_5(s) = X_4(s)\cos(2\widehat{\omega}_{me} - \omega_h t)$ and $Y_5(s) = Y_4(s)\sin(2\widehat{\omega}_{me} - \omega_h t)$. Particularly, defining ω_d as the difference between the injection pulsation frequency and two times the estimated electromechanical speed, i.e. $\omega_d = \omega_h - 2\widehat{\omega}_{me}$, the Laplace transform of the signal $\epsilon'(s) = F_{\mathrm{LPF}}(s)[X_5(s) + Y_5(s)]$ is:

$$\begin{aligned} \epsilon'(s) = F_{\mathrm{LPF}}(s)[&F_{\mathrm{HPF}}(s-j\omega_d)(\delta_1+\delta_2) \dots \\ &+ F_{\mathrm{HPF}}(s+j\omega_d)(\delta_3+\delta_4)] \end{aligned} \tag{5.6}$$

where:

$$\begin{aligned} \delta_1 &= U_\alpha(s-j\omega_d)G_\Sigma(s-j(\omega_d+\omega_{me}))/4 \dots \\ &\quad + jU_\beta(s-j\omega_d)G_\Sigma(s-j(\omega_d+\omega_{me}))/4, \\ \delta_2 &= U_\alpha(s-j(\omega_d+2\omega_{me}))G_\Delta(s-j(\omega_d+\omega_{me}))/4 \dots \\ &\quad - jU_\beta(s-j(\omega_d+2\omega_{me}))G_\Delta(s-j(\omega_d+\omega_{me}))/4, \\ \delta_3 &= U_\alpha(s+j\omega_d)G_\Sigma(s+j(\omega_d+\omega_{me}))/4 \dots \\ &\quad - jU_\beta(s+j\omega_d)G_\Sigma(s+j(\omega_d+\omega_{me}))/4, \\ \delta_4 &= U_\alpha(s+j(\omega_d+2\omega_{me}))G_\Delta(s+j(\omega_d+\omega_{me}))/4 \dots \\ &\quad + jU_\beta(s+j(\omega_d+2\omega_{me}))G_\Delta(s+j(\omega_d+\omega_{me}))/4. \end{aligned} \tag{5.7}$$

Neglecting the resistive contribution to the injection frequency and remembering that the Laplace transforms of the injected sine and cosine signals in (2.9) are $U_\alpha(s) = U_h s/(s^2+{\omega_h}^2)$ and $U_\beta(s) = U_h\omega_h/(s^2+{\omega_h}^2)$. The signal δ_1 can be written in the Laplace-domain as follows:

$$\delta_1 = \frac{U_h l_\Sigma}{2 l_{dd} l_{qq}} \left\{ \frac{1}{s - j\omega_h} \left[\frac{s - j(\omega_h - 2\widehat{\omega}_{me})}{\omega_h^2 + (s - j(\omega_h - 2\widehat{\omega}_{me}))^2} \cdots + \frac{j\omega_h}{\omega_h^2 + (s - j(\omega_h - 2\widehat{\omega}_{me}))^2} \right] \right\} \tag{5.8}$$

where in G_Σ only the injection pulsation ω_h is considered since ω_{me} and $\widehat{\omega}_{me}$ can be neglected. Hence, (5.8) can be rearranged to highlight that it is composed by four sinusoidal waves, namely:

$$\delta_1 = \frac{U_h l_\Sigma}{2 l_{dd} l_{qq}} \cdot \frac{1}{\omega_h - 2\widehat{\omega}_{me}} \left[-\frac{\omega_h}{s^2 + \omega_h^2} + \frac{2(\omega_h - \widehat{\omega}_{me})}{s^2 + 4(\omega_h - \widehat{\omega}_{me})^2} \cdots + \frac{js}{s^2 + \omega_h^2} - \frac{js}{s^2 + 4(\omega_h - \widehat{\omega}_{me})^2} \right]. \tag{5.9}$$

Two components are at the injection frequency while the other two are at $(2\omega_h - \widehat{\omega}_{me})$, which are greater than the low-pass filter cutoff frequency, so they are filtered.

The same procedure can be adopted for the signal δ_2 which is composed by four sinusoidal waves at the pulsation of $2\widetilde{\omega}_{me}$ and ω_h, namely:

$$\delta_2 = \frac{U_h l_\Delta}{2 l_{dd} l_{qq}} \cdot \frac{1}{\omega_h - 2\widetilde{\omega}_{me}} \left[\frac{2\widetilde{\omega}_{me}}{s^2 + 4\widetilde{\omega}_{me}^2} - \frac{\omega_h}{s^2 + \omega_h^2} \cdots - \frac{js}{s^2 + 4\widetilde{\omega}_{me}^2} + \frac{js}{s^2 + \omega_h^2} \right] \tag{5.10}$$

where $\widetilde{\omega}_{me}$ is defined as the speed error $\widetilde{\omega}_{me} = \omega_m - \widehat{\omega}_{me}$. After filtering it with the LPF, the terms around the injection frequency ω_h are suppressed. Finally, noting that:

$$\mathcal{L}^{-1}\left(\frac{2\widetilde{\omega}_{me}}{s^2 + 4\widetilde{\omega}_{me}^2} \right) = \sin(2\widetilde{\omega}_{me} t) = \sin(2\Delta\vartheta) \tag{5.11}$$

linearizing it for small estimation error and repeating the same procedure for δ_3 and δ_4, the expression in the Laplace-domain of the signal ϵ' is found:

$$\epsilon'(s) = \frac{2U_h l_\Delta}{\omega_h l_{dd} l_{qq}} F^\Sigma_{\mathrm{HPF}}(s) F_{\mathrm{LPF}}(s)(\vartheta_{me}(s) - \widehat{\vartheta}_{me}(s) - j) \tag{5.12}$$

where:

$$F^\Sigma_{\mathrm{HPF}}(s) = \frac{1}{2}(F_{\mathrm{HPF}}(s + j\omega_d) + F_{\mathrm{HPF}}(s - j\omega_d)). \tag{5.13}$$

As a consequence the new estimator TF is:

$$P^{\mathrm{new}}_{\mathrm{obs}}(\mathrm{s}) = \frac{\epsilon'(s)}{\widehat{\vartheta}_{me}(s)} = \frac{2U_h l_\Delta}{\omega_h l_{dd} l_{qq}} F_{\mathrm{LPF}}(s) F^\Sigma_{\mathrm{HPF}}(s) \tag{5.14}$$

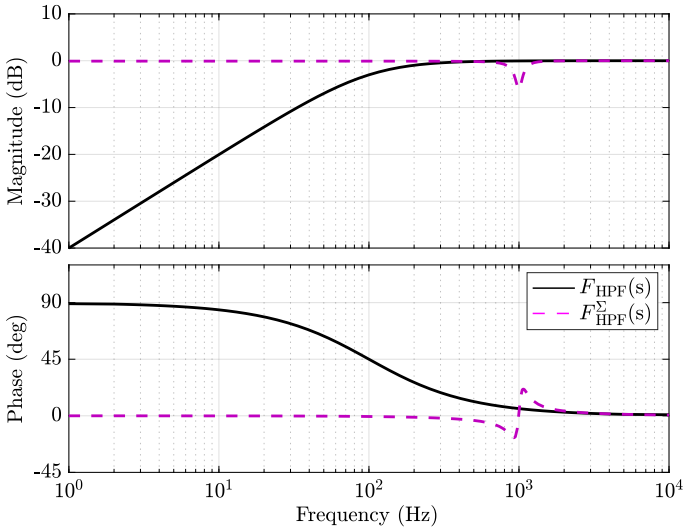

Figure 5.3: Bode plot of the conventional high-pass filter TF $F_{\mathrm{HPF}}(s)$ and the proposed representation $F^{\Sigma}_{\mathrm{HPF}}(s)$.

which differs from the conventional one (5.2) both in the frequency behaviour and for a generalized static gain. At low-speed or standstill, ω_h is greater than the estimated electrical pulsation, then $\omega_d \simeq \omega_h$.

The frequency response of the conventional and the new high-pass filter TFs is shown in Fig. 5.3.

The cutoff frequency is set to 100 Hz. A significant difference can be noted in the low-frequency range where the two TF differs both in magnitude and in phase. The low-frequency range behaviour due to the different high-pass filter TFs is a crucial point in the observer design. A different high-pass filter TF changes the observer TF and this leads both to a different regulators tuning and observer performance. Furthermore, the proposed $F^{\Sigma}_{\mathrm{HPF}}(s)$ is akin to a slight notch filter behaviour at the injection pulsation ω_h with a sag depth equal to -6 dB.

The $F^{\Sigma}_{\mathrm{HPF}}(s)$ TF is the model description of the conventional high-pass filter taking into account the demodulation process obtained in the Laplace-domain. The high pass filter TF in the conventional approach has the function to isolate the high frequency component of the measured currents in the stationary reference frame. By doing so, since time and Laplace domain variables are mixed in the conventional approach, the translation in the frequency domain is not correct and the demodulation effects are not properly considered. A wrong stability analysis and an inaccurate bandwidth are the result of neglecting the TF frequency shift due to the modulation/demodulation process. This difference leads to a wrong observer model, hence a proper estimator regulator can not be designed, especially in the low-frequency range. Finally, it is worth remembering that the discretization of $F_{\mathrm{HPF}}(s)$ is actually implemented

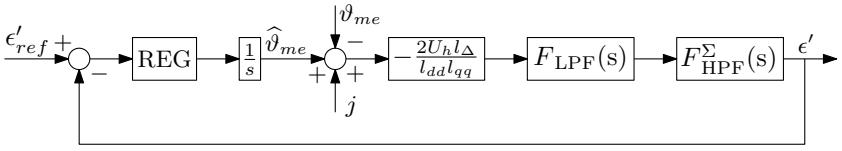

Figure 5.4: Observer control-loop of a rotating injection sensorless drive with the proposed high-pass filter TF.

in the position observer with the demodulation process, whereas $F^{\Sigma}_{\mathrm{HPF}}(s)$ is its model and it is used to design the estimator regulator.

5.2 Observer Regulator Design

The design of the observer regulator in a sensorless electric drive is crucial to guarantee the motor drive stability and performance. The observer CL interacts with current and speed loops, then an accurate tuning must be carried out to reach both high disturbance rejection and a wide closed loop bandwidth. The observer CL is shown in Fig. 5.4 where the actual position acts a disturbance as well as the complex term j. Two tuning approaches are tested, namely, the direct synthesis and the internal model principle with Bode's synthesis.

5.2.1 Direct Synthesis Tuning

The DS method is a controller tuning method able to consider systems with a nonunitary feedback. Moreover the regulator is designed to achieve a desired closed loop TF. Let $\mathrm{R(s)}$, $\mathrm{P(s)}$ and $\mathrm{F(s)}$ be the TFs of the regulator, the plant and filter on the feedback of a negative control-loop, respectively. With the variables just defined, the closed loop TF $\mathrm{W(s)}$ is:

$$W(s) = \frac{R(s)P(s)}{1 + R(s)P(s)F(s)} \tag{5.15}$$

Particular attention should be given to the desired CL function $\mathrm{W^*(s)}$ since it must guarantee the synthesis of a feasible regulator. In this case, a second order TF must be chosen, as:

$$W^*(s) = \frac{\omega_{obs}^2}{s^2 + 2\omega_{obs}\xi_{obs}s + \omega_{obs}^2} \tag{5.16}$$

where ω_{obs} is the desired bandwidth of the observer and $\xi_{obs} = 1/\sqrt{2}$ is the critical damping factor which allow having a -3 dB gain at ω_{obs}. So, from the closed loop TF of the system, the regulator TF can be found as:

$$R(s) = \frac{W^*(s)}{P(s)[1 - F(s)W^*(s)]}. \tag{5.17}$$

The DS regulator allow easily verifying the accuracy of the proposed TF. The system response both in time and frequency domain is the same if the actual TF matches the proposed one. The main problem of the DS method is its poor disturbance rejection.

5.2.2 Internal Model Principle

The disturbance rejection of a feedback system is assured by the IMP if the open loop TF includes the disturbance model. Fig. 5.4 shows the observer control-loop of a rotating injection sensorless drive. At steady-state condition, the actual position acts as a ramp-varying disturb that must be rejected. A PI controller together with the integrator already present in the observer control-loop can satisfy the required criteria about the disturbance rejection. However, the IMP method is based on a desired open loop TF, hence the CL response cannot guarantee a fine control as with the DS method.

5.2.3 Comparison Between Observer Regulators

The aim of the proposed observer control-loop design is to achieve an accurate control of the system bandwidth. Two regulators are obtained using the DS and the IMP techniques both with a desired CL bandwidth of $\omega_{obs} = 50\,\mathrm{Hz}$ and a phase margin of 70° for the regulator based on the IMP. Fig. 5.5 shows the comparison between the regulators.

Provided a suitable $\mathrm{W}^*(\mathrm{s})$, the DS method is always able to synthesize a feasible regulator. Moreover, if the actual TF is equal to the proposed one $P_{\mathrm{obs}}^{\mathrm{new}}(\mathrm{s})$, the obtained CL bandwidth is equal to the desired one. The IMP approach, set the OL cross-over frequency and it assumes that it is equal to the closed loop bandwidth. Hence, the transient response of the CL system it is not the desired one as it will shown in Section 5.3.

5.3 Results

Two different tests are carried out to prove the accuracy of the proposed observer TF compared to the conventional one. The tests are performed on an IPM, whose parameters are reported in Tab. 5.1. The sensorless drive parameters are listed in Tab. 5.2. The current and speed control loops bandwidth are set to $100\,\mathrm{Hz}$ and $10\,\mathrm{Hz}$, respectively. In Section 5.3.1 the feasibility and the time response of the observer TF is studied. Both DS and IMP approaches are used to design different regulators with the conventional observer TF and the proposed one. In Section 5.3.2 the IMP approach is used to study the position tracking response in time-domain of two regulators designed by using the conventional observer TF and the proposed one. All the presented result are done in simulation environment.

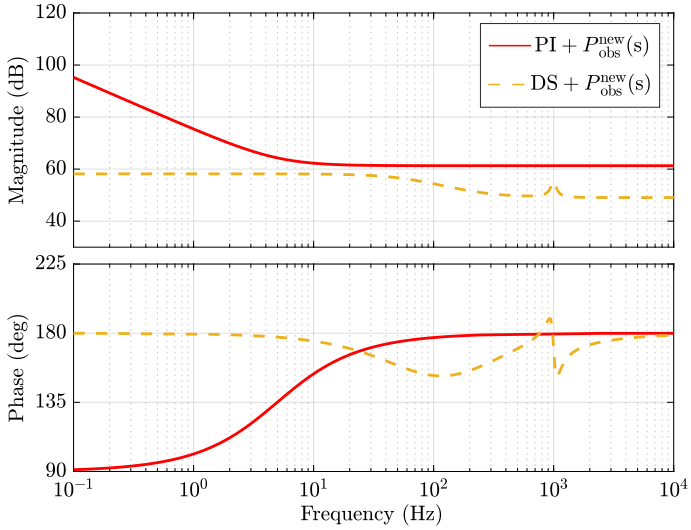

Figure 5.5: TF of the observer regulators designed with the DS and the IMP approaches.

Table 5.1: Main motor parameters.

Parameter	Symbol	Value
Resistance	R_s	$2.726\,\Omega$
d-axis inductance	L_d	$26.5\,\text{mH}$
q-axis inductance	L_q	$114.7\,\text{mH}$
Permanent magnet	λ_{mg}	$0.22\,\text{V s}$
Nominal current	I_N	$4.2\,\text{A}$
Nominal torque	T_N	$4.7\,\text{N m}$
Rated speed	ω_N	$3000\,\text{rpm}$

5.3.1 Observer Time Response

Different controllers with DS and IMP methods are designed with several desired CL bandwidth and by exploiting the two observer TF models. The aim of the test is to verify the feasibility of the regulators and to prove the effectiveness of the proposed observer TF compared to the existing approach. Results of some combinations of required bandwidth and type of designed regulators are bundled in Tab. 5.3, the stable combinations are marked. A stable behaviour for all the considered bandwidth is achieved by the DS method with the proposed observer TF $P_{\text{obs}}^{\text{new}}(\text{s})$ proving that the observer is well described. Regulators designed with the proposed TF and the IMP approach shows a stable behaviour for OL bandwidth from $10\,\text{Hz}$ to $50\,\text{Hz}$. Stable low-frequency response confirms the effectiveness of (5.14). Whereas, an unstable behaviour appears for large desired observer bandwidth. This behaviour is

Table 5.2: Sensorless drive parameters.

Parameter	Symbol	Value
Injection frequency	f_h	1000 Hz
Injection magnitude	U_h	60 V
HPF cutoff frequency	f_H	100 Hz
LPF cutoff frequency	f_L	200 Hz

due to the IMP design method that imposes only the OL bandwidth. As a consequence the closed loop one is always greater than the imposed one. If a too large actual bandwidth results, the system becomes unstable. Regulators designed both with DS and IMP approaches and the conventional $P_{\mathrm{obs}}^{\mathrm{old}}(\mathrm{s})$ shows a stable behaviour only at high frequencies where the $F_{\mathrm{HPF}}(s)$ in the observer model coincides with the proposed one $F_{\mathrm{HPF}}^{\Sigma}(s)$ as shown in Fig. 5.3. The $P_{\mathrm{obs}}^{\mathrm{new}}(\mathrm{s})$ is the proposed observer TF where $F_{\mathrm{HPF}}^{\Sigma}(s)$ is retrieved by considering the modulation/demodulation effects on the high-pass filter TF in the Laplace-domain. The different description of the conventional approach is responsible for the unstable behaviour of the regulator designed with $P_{\mathrm{obs}}^{\mathrm{old}}(\mathrm{s})$ in the low frequency range.

The transient response to a step reference of $\epsilon'_{ref} = 0.1\,\mathrm{rad}$ applied at $t = 0.01\,\mathrm{ms}$ is studied to prove the dynamic behaviour of all the obtained feasible regulators. The results are shown in Fig. 5.6. The desired CL response ϵ'_{W^*} is obtained by applying ϵ'_{ref} on (5.16). It is worth remembering that if the plant is well described, the measured ϵ' perfectly overlaps with the theoretical one ϵ'_{W^*}. Hence, the desired response of the regulator is perfectly obtained. The controllers designed with the DS approach and the proposed $P_{\mathrm{obs}}^{\mathrm{new}}(\mathrm{s})$ allow achieving a CL response of the observer TF that is perfectly overlapped to the theoretical step response to the closed loop TF reported in (5.16) for all the chosen bandwidth. Hence, the proposed plant description is accurate. The closed loop responses obtained using the DS method to synthesize the controller and the conventional observer TF $P_{\mathrm{obs}}^{\mathrm{old}}(\mathrm{s})$ are not always feasible. The flaws of the conventional approach are highlighted especially in the low-frequency range, leading to instability issues if a reduced bandwidth is desired. Finally, it is worth noting that PIs tuning are not feasible for all the desired bandwidth and that PIs tuned with (5.2) are not feasible in the low-frequency range. Moreover, the transient behaviour of all the PIs is faster than the desired one. The faster transient response of the regulators designed with the IMP approach is responsible for the unstable behaviour at high-frequency of the PIs designed with $P_{\mathrm{obs}}^{\mathrm{new}}(\mathrm{s})$ as shown in Tab. 5.3. The open loop TF is used by the IMP approach to design the regulators, hence an high open loop cut-off frequency results in an higher CL bandwidth not sustainable by the observer.

Table 5.3: Stable observer combinations as a function of the required bandwidth.

	10 Hz	30 Hz	50 Hz	100 Hz	150 Hz
DS + $P_{\text{obs}}^{\text{new}}(\text{s})$	✓	✓	✓	✓	✓
DS + $P_{\text{obs}}^{\text{old}}(\text{s})$				✓	✓
PI + $P_{\text{obs}}^{\text{new}}(\text{s})$	✓	✓	✓		
PI + $P_{\text{obs}}^{\text{old}}(\text{s})$			✓	✓	✓

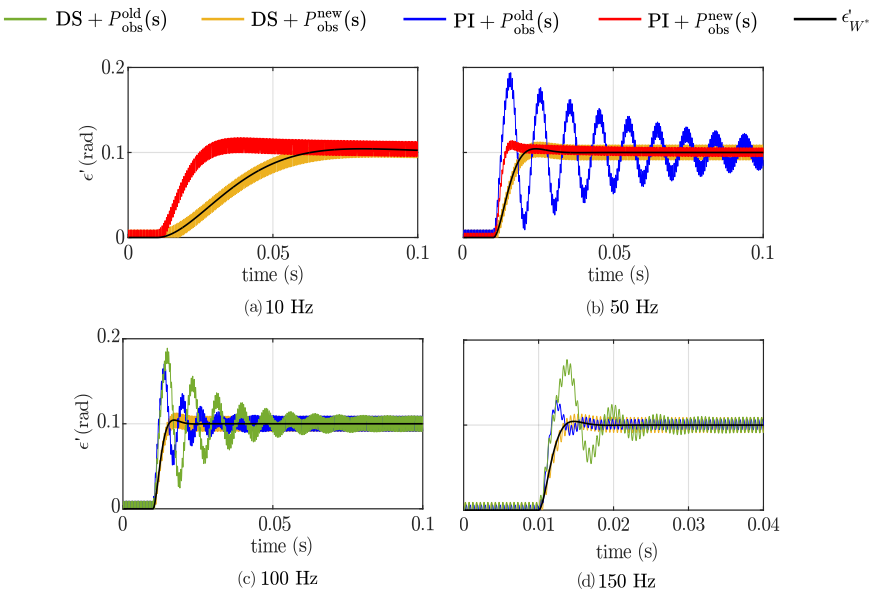

Figure 5.6: Observer response to a step reference of ϵ'_{ref} of all synthesized regulator listed in Tab. 5.3 and comparison with the nominal response ϵ'_{W^*}.

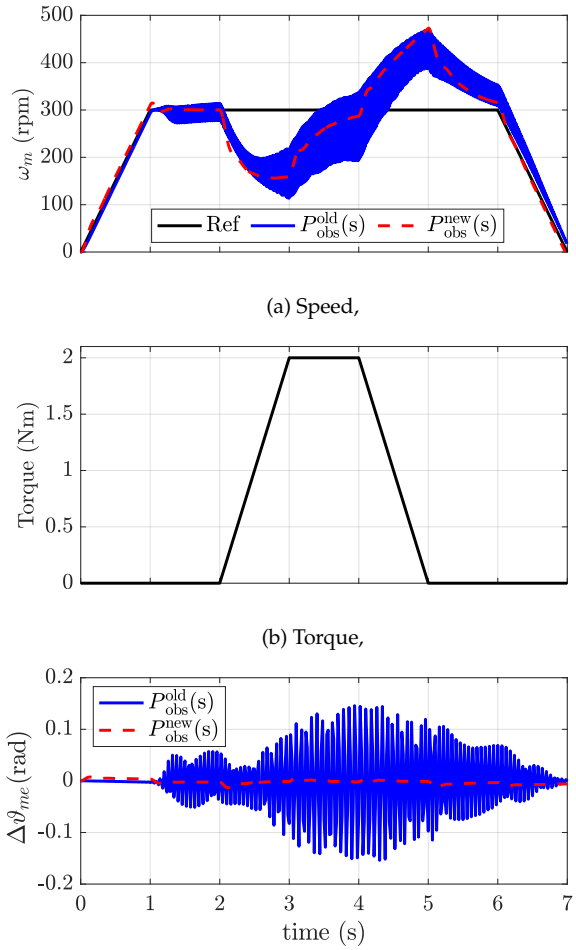

(a) Speed,

(b) Torque,

(c) Position error,

Figure 5.7: Closed loop dynamic test. Two regulators are designed with the IMP approach with a desired bandwidth of 40 Hz and a phase margin of 75° by using the conventional $P_{\text{obs}}^{\text{old}}(\text{s})$ and the proposed $P_{\text{obs}}^{\text{new}}(\text{s})$ observer TFs.

5.3.2 Position Tracking

In this test two different regulators are designed with the IMP approach using both the conventional TF $P_{\text{obs}}^{\text{old}}(\text{s})$ and the proposed one $P_{\text{obs}}^{\text{new}}(\text{s})$.

The desired closed loop bandwidth is set to 40 Hz with a phase margin of 75° for both regulators. The test are performed with the motor operating sensorless. The regulators are designed to highlight the flaws of the conventional approach compared to the proposed one regarding the position tracking. Current and speed loops are closed on the estimated position and speed, respectively. A ramp speed reference of 300 rpm and a torque rampwise disturbance of 2 N m are applied at the motor shaft as shown in Fig. 5.7a and Fig. 5.7b.

The performance of the designed position observers is studied by means of the position error $\Delta\vartheta_{me}$ as shown in Fig. 5.7c. The PI tuned with $P_{\text{obs}}^{\text{new}}(\text{s})$ shows a position error that is almost zero and it able to fully reject the actual position disturbance. An initial stable behaviour is shown by the PI designed with $P_{\text{obs}}^{\text{old}}(\text{s})$, however when the ramp-wise speed reference reaches its nominal value at $1\,\text{s}$, the CL response of the system is almost unstable according to the transient analysis pointed out in Section 5.3.1. Furthermore, when the load is applied the peak value of $\Delta\vartheta_{me}$ is about $0.15\,\text{rad}$ leading to a detrimental performance of the electric drive. Finally, the operating conditions of the test show the effectiveness of the proposed approach. Indeed, the observer designed with the proposed TF allow controlling the motor sensorless with up to 10% of its nominal speed and with a torque disturb of about 50% of the nominal one.

The inaccuracy in the description of the observer TF due to the use of time and Laplace-domain variables makes impossible to design a regulator in the low-frequency range with $P_{\text{obs}}^{\text{old}}(\text{s})$ according to the analysis carried out in Tab. 5.3.

5.4 Conclusion

A new transfer function model for rotating injection-based position observer by exploiting the modulation/demodulation theory is proposed. The conventional TF blends together time and Laplace-domain variables neglecting demodulation effects on the high-pass filter TF. The proposed plant description differs from the classical one for a different high-pass filter function due to the demodulation process. The main difference between the conventional and the proposed observer TF is in the low-frequency response.

Several regulators were obtained with different bandwidth and by using two design approaches, namely, direct synthesis and internal model principle. The former approach allow achieving a desired closed loop bandwidth if a proper transfer function is provided. The transient response of different regulators is compared to the theoretical one obtained by applying a step reference to the desired closed loop TF according to the DS approach. The regulators designed with the proposed observer TF perfectly match the theoretical response, confirming the correctness of the proposed observer model. In the second test, two different regulators with the internal model principle are designed at low frequency. Sensorless control is performed and the performance of the two regulators compared. The regulator designed by using the conventional observer TF is almost unstable, whereas the PI designed with the proposed observer TF perfectly attains the desired behaviour.

6 General Conclusion

Electric motors have a fundamental role in the electrification process. Following the upcoming regulations in terms of climate change and energy savings, in the next years electric motors are going to gain more and more importance in several sectors such as industrial, transportation and domestic. Efficiency, reduced size of the motor and fault-tolerant capability for instance are going to be key specifications both on motor and electric drive design. Already today, for instance, electric motors are one of the biggest energy consumers in the world due to their wide use in the aforementioned sectors. In these scenario, in the field of electric drives, a lot can be done by investigating different control techniques.

In this thesis, low speed sensorless control is deeply investigated both for three-phase and multiphase machines. The reason is that by implementing motor control algorithms without position sensor, most of the design specifications can be satisfied. Sensorless control allow achieving redundancy and fault-tolerant capability if a fault in the position sensor appears. Moreover, a reduced cost and motor frame size can by satisfied by removing the position sensor. However, sensorless control suffers from magnetic saturation and cross coupling. The former one reduces the motor anisotropy creating a problem in the low speed region since the rotor position is retrieved by depicting the anisotropy of the motor. If the anisotropy is reduced, for instance when the motor operates at high current, the estimated position can be detrimental and not correct. The latter one introduces an estimation error, hence the rotor position may differ from the actual one. These aforementioned flaws modify the actual operating point of the machine when sensorless control is applied. Inaccuracy of the model is another key factor that can undermine the performance of sensorless control. Model based design is often used to model the position observer used to retrieve the rotor position. Hence, efficiency problems and even instability issues could arise. Low speed sensorless control is investigated for different electric motors.

The first part deals with low speed sensorless control applied for a multiphase machine. The reference scenario is a fault in the position sensor. The winding arrangement is chosen accordingly to control the machine as a dual three-phase motor. One three phase winding is distributed at the top of the stator whereas the second one at the bottom. Both three-phase winding are supplied with a dedicated inverter. This allow both controlling each set at different operating points and the estimation of two rotor positions. The ability of the motor to be controlled sensorless is investigated in the first work. A full study of the motor is carried out both with finite element analysis and simulation tools and experimental validation. Observer trajectories are depicted in the dq plane and through their study a sensorless control that enhances the

fault-tolerant of the motor is designed. An investigation of sensor fusion application to perform sensorless control is reported in the second study. The rotor position is estimated by both winding sets. As aforementioned, the accuracy of the estimated position depends on the operating point of the machine. Hence, since the two three-phase sets can be controlled at different operating points, this results in two different estimated positions. Depending on the operating point of the machine, one estimated position may have more relevance than another one. Sensor fusion aims at combining together the two estimated rotor positions to have only one estimated and properly weighted variable. Sensorless control is finally performed by closing both control loops on the fused state from the Kalman filter algorithm showing good performance.

The second part of the thesis deals with the third study. It is related on the modelling of a position observer for the rotating voltage signal injection. The proposed approach aims at modelling the observer plant completely in the Laplace domain. The novelty of the study is that the demodulation effects on the filters transfer functions are considered. As a consequence, a correct observer plant is obtained compared to the conventional approach that blends together time and Laplace domain variables. The correctness of the proposed observer transfer function is validated through simulation results. As a result, the tuning of the observer regulator can be done by using model based techniques such as direct synthesis or the internal model principle. The proposed approach allow reaching an optimal tuning of the regulator in the whole frequency range whereas by using the conventional one only a tuning at high frequency range is possible. Moreover, the reached performance are not the same as the required one since an incorrect plant is used.

6.1 Future Works

Low speed and standstill sensorless control with rotating injection technique has been deeply investigated in the dissertation both for three-phase and multiphase machines. However, the activities reported may have multiple development or interesting insight to investigate.

Further improvements can be implemented on the post fault tolerant strategies developed for the multiphase motor in the first part of the thesis. The effects of the $Q-PLL$ tuning on the slightly variation on the estimated position can be investigated. Moreover, a different configuration of the stator windings can be used to highlight and investigate the effect of the mutual coupling between the multiple three-phase sets on the estimated position. Finally, pulsating injection techniques can be implemented to analyze the differences in the control strategy compared to the rotating one that was implemented.

An experimental verification of the work carried out regarding the modelling of a position observer for rotating voltage signal injection should be

done to validate the simulation results. Moreover, further validation on the influence of the motor speed on the observer plant is needed. Finally, a comparison between the observer plant of the rotating and pulsating injection techniques could be performed to highlight the differences.

ACKNOWLEDGEMENT

These three years were not an easy and linear road. I started the PhD journey as soon as I graduated and as all novel master students graduates, I though I had all the answers. It took me a while to understand that I had to do one step back, to do two steps in front. These three years helped me to be more focus and to keep attention to these little details that in research, as in life, makes the biggest importance. I will always be grateful for the open-mindedness that this journey gave me.

Said that, I want to thank the people that shared these amazing journey with me. People without whom, these experience would not have been the same. Thank you *Paolo*, *Andrea*, *Chiara*, *Alice*, *Diego*, *Luca* and *Mosè*. Like every experience, with some people you share more than others.

A big thanks to my "socio", *Elia Scolaro*. We have known each other for almost 8 years now. I remember the first day of the Bachelor degree, I was not even sure to pass the first year. Feeling almost out of contest with all that math. Now here we are, discussing about what to put inside the PhD thesis. Thank you my friend for all the laughing, free dinners at your home and car sharing.

Then, I want to thank *Matteo Beligoj* and *Daniele Michieletto*. Together with *Elia* we are the EDLab Sharks. We did an incredible journey with that challenge and I will always remember our team work as one of the best experience ever.

Thank you *Nicola Bianchi* for your precious tips.

A big thanks to my supervisor *Luigi Alberti*. We work together since my bachelor degree and its quite funny but actually you were my supervisor for all my dissertations. It was incredible starting from a scratch idea and build up a master degree course from zero. I will always remember our afternoons before every lesson of the first year of the course and our little Monte Pelmo walk this summer.

Many thanks to my co-supervisor *Ludovico Ortombina*. I learned a lot from you. Thank you for your patience and help with all the projects we have worked together. Last but not least, my whole family.

Thank you Dad, *Maurizio* and Mom, *Rosamaria* for watching me grow from the back. *Adriana*, *Andrea*, *Aurora* and *Desirée* this is for you. Do not feel accomplished about anything. Keep not only dreaming but even commit yourself to reach your goals. *Carlo*, I do not know if you can come to Prague... Now, as every discussion we had and we will have I am going to tell you "How many *100* do you have?"

Thank you *Sara*, for being my first love. If today I am here, it is even because you ever supported me, despite everything. We shared a lot since high school and you will be ever be part of me. All the best for your future, because even if our journey now is different I will ever be your best supporter.

Thank you *Lina*, *Stefano* and all *Pizzeria allo Scricchio*. You are my second family.

It was not an easy journey and you all know it. But we did it. All of you have always wanted my best and I think that in terms of perseverance and determination, this is a good result.

Giuseppe.

PUBLICATIONS

G. Galati, L. Ortombina, L. Alberti and M. Berto, "Investigation on the Self-Sensing Capability of a Dual Three-Phase Synchronous Reluctance Machine," 2022 International Conference on Electrical Machines (ICEM), Valencia, Spain, 2022, pp. 2256-2262, doi: 10.1109/ICEM51905.2022.9910871.

G. Galati, L. Ortombina, L. Alberti and M. Berto, "Improved Sensorless Control of Multiphase Synchronous Reluctance Machine Under Position Sensor Fault," in IEEE Journal of Emerging and Selected Topics in Industrial Electronics, doi: 10.1109/JESTIE.2023.3294100.

G. Galati, L. Ortombina and L. Alberti, "Modelling of a Rotating Signal Injection-Based Position Observer for Sensorless Synchronous Electric Drives," 2023 IEEE International Electric Machines & Drives Conference (IEMDC), San Francisco, CA, USA, 2023, pp. 1-7, doi: 10.1109/IEMDC55163.2023.10238996.

G. Galati, L. Alberti, L. Ortombina, "Fault-Tolerant Analysis of Kalman Filter Sensor Fusion for Sensorless Control of a Multiphase Machine," 2023 IEEE 14th International Symposium on Diagnostics for Electrical Machines, Power Electronics and Drives (SDEMPED), Chania, Greece, 2023, , pp. 147-153, doi: 10.1109/SDEMPED54949.2023.10271448.

G. Galati, E. Scolaro, D. Michieletto, M. Beligoj, L. Ortombina, "Motor Vehicle Challenge 2023: The Winning Multi-physical Energy Management Algorithm," 2023 IEEE Vehicle Power and Propulsion Conference (VPPC), Milan, Italy, 2023.

BIBLIOGRAPHY

[1] M. Corley and R. Lorenz, "Rotor position and velocity estimation for a salient-pole permanent magnet synchronous machine at standstill and high speeds," *IEEE Transactions on Industry Applications*, vol. 34, no. 4, pp. 784–789, 1998.

[2] A. Salem and M. Narimani, "A review on multiphase drives for automotive traction applications," *IEEE Transactions on Transportation Electrification*, vol. 5, pp. 1329–1348, dec 2019.

[3] R. Bojoi, S. Rubino, A. Tenconi, and S. Vaschetto, "Multiphase electrical machines and drives: A viable solution for energy generation and transportation electrification," in *2016 International Conference and Exposition on Electrical and Power Engineering (EPE)*, IEEE, oct 2016.

[4] I. Zoric, M. Jones, and E. Levi, "Arbitrary power sharing among three-phase winding sets of multiphase machines," *IEEE Transactions on Industrial Electronics*, vol. 65, pp. 1128–1139, feb 2018.

[5] L. Parsa and H. Toliyat, "Five-phase permanent-magnet motor drives," *IEEE Transactions on Industry Applications*, vol. 41, pp. 30–37, jan 2005.

[6] Y. Hu, Z. Q. Zhu, and M. Odavic, "Comparison of two-individual current control and vector space decomposition control for dual three-phase PMSM," *IEEE Transactions on Industry Applications*, vol. 53, pp. 4483–4492, sep 2017.

[7] E. Levi, "Advances in converter control and innovative exploitation of additional degrees of freedom for multiphase machines," *IEEE Transactions on Industrial Electronics*, vol. 63, pp. 433–448, jan 2016.

[8] O. Lopez, J. Alvarez, J. Malvar, A. G. Yepes, A. Vidal, F. Baneira, D. Perez-Estevez, F. D. Freijedo, and J. Doval-Gandoy, "Space-vector PWM with common-mode voltage elimination for multiphase drives," *IEEE Transactions on Power Electronics*, vol. 31, pp. 8151–8161, dec 2016.

[9] Ó. Lopez, J. Alvarez, J. Doval-Gandoy, and F. D. Freijedo, "Multilevel multiphase space vector PWM algorithm," *IEEE Transactions on Industrial Electronics*, vol. 55, pp. 1933–1942, may 2008.

[10] O. Lopez, J. Alvarez, A. G. Yepes, F. Baneira, D. Perez-Estevez, F. D. Freijedo, and J. Doval-Gandoy, "Carrier-based PWM equivalent to multilevel multiphase space vector PWM techniques," *IEEE Transactions on Industrial Electronics*, vol. 67, pp. 5220–5231, jul 2020.

[11] A. Mohammadpour and L. Parsa, "Global fault-tolerant control technique for multiphase permanent-magnet machines," *IEEE Transactions on Industry Applications*, vol. 51, pp. 178–186, jan 2015.

[12] S. Dwari and L. Parsa, "An optimal control technique for multiphase PM machines under open-circuit faults," *IEEE Transactions on Industrial Electronics*, vol. 55, pp. 1988–1995, may 2008.

[13] F. Meinguet, N.-K. Nguyen, P. Sandulescu, X. Kestelyn, and E. Semail, "Fault-tolerant operation of an open-end winding five-phase PMSM drive with inverter faults," in *IECON 2013 - 39th Annual Conference of the IEEE Industrial Electronics Society*, IEEE, nov 2013.

[14] R. Nelson and P. Krause, "Induction machine analysis for arbitrary displacement between multiple winding sets," *IEEE Transactions on Power Apparatus and Systems*, vol. PAS-93, pp. 841–848, may 1974.

[15] I. Zoric, M. Jones, and E. Levi, "Vector space decomposition algorithm for asymmetrical multiphase machines," in *2017 International Symposium on Power Electronics (Ee)*, IEEE, oct 2017.

[16] S. Rubino, R. Bojoi, F. Mandrile, and E. Armando, "Modular stator flux and torque control of multiphase induction motor drives," in *2019 IEEE International Electric Machines & Drives Conference (IEMDC)*, IEEE, may 2019.

[17] S. Rubino, R. Bojoi, E. Levi, and O. Dordevic, "Vector control of multiple three-phase permanent magnet motor drives," in *IECON 2018 - 44th Annual Conference of the IEEE Industrial Electronics Society*, IEEE, oct 2018.

[18] S. Rubino, O. Dordevic, R. Bojoi, and E. Levi, "Modular vector control of multi-three-phase permanent magnet synchronous motors," *IEEE Transactions on Industrial Electronics*, vol. 68, pp. 9136–9147, oct 2021.

[19] S. Rubino, O. Dordevic, E. Armando, I. R. Bojoi, and E. Levi, "A novel matrix transformation for decoupled control of modular multiphase PMSM drives," *IEEE Transactions on Power Electronics*, vol. 36, pp. 8088–8101, jul 2021.

[20] J. Liu and Z. Zhu, "Rotor position estimation for dual-three-phase permanent magnet synchronous machine based on third harmonic back-EMF," in *2015 IEEE Symposium on Sensorless Control for Electrical Drives (SLED)*, IEEE, jun 2015.

[21] S. Bolognani, S. Calligaro, and R. Petrella, "Design issues and estimation errors analysis of back-EMF based position and speed observer for SPM synchronous motors," in *2011 Symposium on Sensorless Control for Electrical Drives*, IEEE, sep 2011.

[22] Y. Zhao, Z. Zhang, W. Qiao, and L. Wu, "An extended flux model-based rotor position estimator for sensorless control of salient-pole permanent-magnet synchronous machines," *IEEE Transactions on Power Electronics*, vol. 30, pp. 4412–4422, aug 2015.

[23] I. Boldea, M. C. Paicu, and G.-D. Andreescu, "Active flux concept for motion-sensorless unified AC drives," *IEEE Transactions on Power Electronics*, vol. 23, pp. 2612–2618, sep 2008.

[24] J.-H. Jang, J.-I. Ha, M. Ohto, K. Ide, and S.-K. Sul, "Analysis of permanent-magnet machine for sensorless control based on high-frequency signal injection," *IEEE Transactions on Industry Applications*, vol. 40, pp. 1595–1604, nov 2004.

[25] J.-H. Jang, S.-K. Sul, J.-I. Ha, K. Ide, and M. Sawamura, "Sensorless drive of surface-mounted permanent-magnet motor by high-frequency signal injection based on magnetic saliency," *IEEE Transactions on Industry Applications*, vol. 39, pp. 1031–1039, jul 2003.

[26] M. Degner and R. Lorenz, "Using multiple saliencies for the estimation of flux, position, and velocity in AC machines," *IEEE Transactions on Industry Applications*, vol. 34, no. 5, pp. 1097–1104, 1998.

[27] R. Lorenz, "Practical issues and research opportunities when implementing zero speed sensorless control," in *ICEMS'2001. Proceedings of the Fifth International Conference on Electrical Machines and Systems (IEEE Cat. No.01EX501)*, Int. Acad. Publishers, 2001.

[28] A. Maimeri, L. Alberti, and M. Berto, "Fast computation of self-sensing capability of synchronous machines," in *IECON 2022 – 48th Annual Conference of the IEEE Industrial Electronics Society*, IEEE, oct 2022.

[29] A. Maimeri, L. Alberti, S. Bolognani, and M. Berto, "Fast evaluation of self-sensing control capability for a synchronous reluctance motor," in *2022 IEEE Energy Conversion Congress and Exposition (ECCE)*, IEEE, oct 2022.

[30] V. Manzolini and S. Bolognani, "On the rotor position self-sensing capability of IPM and reluctance synchronous motors," in *2018 IEEE 9th International Symposium on Sensorless Control for Electrical Drives (SLED)*, IEEE, sep 2018.

[31] H. Chen, Q. Gao, T. Yang, and M. Sumner, "Fundamental PWM excitation based rotor position estimation for a dual three-phase permanent magnet synchronous machine," *IEEE Journal of Emerging and Selected Topics in Industrial Electronics*, vol. 4, pp. 659–668, apr 2023.

[32] M. Roetzer, U. Vollmer, L. Chen, and R. Kennel, "Anisotropy-based position estimation approach for symmetrical dual three-phase permanent magnet synchronous machines," in *2017 IEEE International Symposium on Sensorless Control for Electrical Drives (SLED)*, IEEE, sep 2017.

[33] X. Bin, X. Luo, L. Zhu, and J. Zhao, "Sensorless control of dual three-phase PMSM with high frequency voltage signal injection," in *2019 22nd International Conference on Electrical Machines and Systems (ICEMS)*, IEEE, aug 2019.

[34] A. H. Almarhoon, Z. Q. Zhu, and P. L. Xu, "Improved pulsating signal injection using zero-sequence carrier voltage for sensorless control of dual three-phase PMSM," *IEEE Transactions on Energy Conversion*, vol. 32, pp. 436–446, jun 2017.

[35] T. Liu, Z. Q. Zhu, Z.-Y. Wu, D. Stone, and M. Foster, "A simple sensorless position error correction method for dual three-phase permanent magnet synchronous machines," *IEEE Transactions on Energy Conversion*, vol. 36, pp. 895–906, jun 2021.

[36] L. Ortombina, D. Pasqualotto, F. Tinazzi, and M. Zigliotto, "Automatic tuning procedure at standstill for extended kalman filter in sensorless control of permanent magnet synchronous motors," in *2019 IEEE 10th International Symposium on Sensorless Control for Electrical Drives (SLED)*, IEEE, sep 2019.

[37] S. Bolognani, L. Tubiana, and M. Zigliotto, "Extended kalman filter tuning in sensorless PMSM drives," in *Proceedings of the Power Conversion Conference-Osaka 2002 (Cat. No.02TH8579)*, IEEE, 2002.

[38] D. E. G. Erazo, O. Wallscheid, and J. Bocker, "Improved fusion of permanent magnet temperature estimation techniques for synchronous motors using a kalman filter," *IEEE Transactions on Industrial Electronics*, vol. 67, pp. 1708–1717, mar 2020.

[39] H. Jafari and J. Poshtan, "Fault isolation and diagnosis of induction motor based on multi-sensor data fusion," in *The 6th Power Electronics, Drive Systems & Technologies Conference (PEDSTC2015)*, IEEE, feb 2015.

[40] R. Doyle and C. Harris, "Multi-sensor data fusion for helicopter guidance using neuro-fuzzy estimation algorithms," in *1995 IEEE International Conference on Systems, Man and Cybernetics. Intelligent Systems for the 21st Century*, IEEE, 1995.

[41] J. Manyika and H. Durrant-Whyte, "On sensor management in decentralized data fusion," in *Proceedings of the 31st IEEE Conference on Decision and Control*, IEEE, 1992.

[42] K. Chang, R. Saha, and Y. Bar-Shalom, "On optimal track-to-track fusion," *IEEE Transactions on Aerospace and Electronic Systems*, vol. 33, pp. 1271–1276, oct 1997.

[43] J. Roecker and C. McGillem, "Comparison of two-sensor tracking methods based on state vector fusion and measurement fusion," *IEEE Transactions on Aerospace and Electronic Systems*, vol. 24, pp. 447–449, jul 1988.

[44] V. Manzolini, M. Morandin, and S. Bolognani, "The crowded axis of the frequency: Optimal pole/zero allocation for a full speed sensorless synchronous motor drives," in *2016 IEEE Energy Conversion Congress and Exposition (ECCE)*, IEEE, sep 2016.

[45] L. Ortombina, D. Pasqualotto, F. Tinazzi, and M. Zigliotto, "Comprehensive analysis and design of a pulsating signal injection-based position observer for sensorless synchronous motor drives," *IEEE Journal of Emerging and Selected Topics in Power Electronics*, vol. 10, pp. 1925–1934, apr 2022.

[46] G. Wang, D. Xiao, G. Zhang, C. Li, X. Zhang, and D. Xu, "Sensorless control scheme of IPMSMs using HF orthogonal square-wave voltage injection into a stationary reference frame," *IEEE Transactions on Power Electronics*, vol. 34, pp. 2573–2584, mar 2019.

[47] Y.-C. Kwon, J. Lee, and S.-K. Sul, "Extending operational limit of IPMSM in signal-injection sensorless control by manipulation of convergence point," *IEEE Transactions on Industry Applications*, vol. 55, pp. 1574–1586, mar 2019.

[48] D. Raca, P. Garcia, D. D. Reigosa, F. Briz, and R. D. Lorenz, "Carrier-signal selection for sensorless control of PM synchronous machines at zero and very low speeds," *IEEE Transactions on Industry Applications*, vol. 46, pp. 167–178, jan 2010.

[49] M. Berto, P. G. Carlet, V. Manzolini, and L. Alberti, "An effective ellipse fitting technique of the current response locus to rotating HF voltage injection in IPMSM for sensorless rotor position estimation," in *IECON 2018 - 44th Annual Conference of the IEEE Industrial Electronics Society*, IEEE, oct 2018.

[50] L. Ortombina, M. Berto, and L. Alberti, "Sensorless drive for salient synchronous motors based on direct fitting of elliptical-shape high-frequency currents," *IEEE Transactions on Industrial Electronics*, vol. 70, pp. 3394–3403, apr 2023.

[51] F. Toso, M. Berto, L. Alberti, and F. Marcuzzi, "Efficient QR updating factorization for sensorless synchronous motor drive based on high

frequency voltage injection," *IEEE Transactions on Industrial Electronics*, vol. 67, pp. 10213–10222, dec 2020.

[52] A. Yousefi-Talouki, P. Pescetto, and G. Pellegrino, "Sensorless direct flux vector control of synchronous reluctance motors including standstill, MTPA, and flux weakening," *IEEE Transactions on Industry Applications*, vol. 53, pp. 3598–3608, jul 2017.

[53] N. Bianchi and S. Bolognani, "Influence of rotor geometry of an IPM motor on sensorless control feasibility," *IEEE Transactions on Industry Applications*, vol. 43, no. 1, pp. 87–96, 2007.

[54] N. Bianchi, E. Fornasiero, and S. Bolognani, "Effect of stator and rotor saturation on sensorless rotor position detection," *IEEE Transactions on Industry Applications*, vol. 49, pp. 1333–1342, may 2013.

[55] M. Berto, L. Alberti, and S. Bolognani, "Experimental investigation on the self-sensing capability of synchronous machines for signal injection sensorless drives," in *2021 IEEE Energy Conversion Congress and Exposition (ECCE)*, IEEE, oct 2021.

[56] M. Berto, L. Alberti, V. Manzolini, and S. Bolognani, "Computation of self-sensing capabilities of synchronous machines for rotating high frequency voltage injection sensorless control," *IEEE Transactions on Industrial Electronics*, vol. 69, pp. 3324–3333, apr 2022.

[57] J.-K. Park, C. Babetto, G. Berardi, J. Hur, and N. Bianchi, "Comparison of fault characteristics according to winding configurations for dual three-phase synchronous reluctance motor," *IEEE Transactions on Industry Applications*, vol. 57, pp. 2398–2406, may 2021.

[58] L. Ortombina, I. Husain, L. Alberti, and N. Bianchi, "Experimental evaluation of flux–weakening capability of dual three-phase synchronous reluctance motor," in *2021 International Aegean Conference on Electrical Machines and Power Electronics & 2021 International Conference on Optimization of Electrical and Electronic Equipment (OPTIM)*, IEEE, sep 2021.

[59] M. Popescu, D. G. Dorrell, L. Alberti, N. Bianchi, D. A. Staton, and D. Hawkins, "Thermal analysis of duplex three-phase induction motor under fault operating conditions," *IEEE Transactions on Industry Applications*, vol. 49, pp. 1523–1530, jul 2013.

[60] C. Babetto, N. Bianchi, A. Torreggiani, C. Bianchini, M. Davoli, and A. Bellini, "Design optimization and analysis of a synchronous reluctance machine for fault-tolerant applications," in *2019 IEEE International Electric Machines & Drives Conference (IEMDC)*, IEEE, may 2019.

[61] E. Armando, R. I. Bojoi, P. Guglielmi, G. Pellegrino, and M. Pastorelli, "Experimental identification of the magnetic model of synchronous machines," *IEEE Transactions on Industry Applications*, vol. 49, pp. 2116–2125, sep 2013.

[62] "Dolomites, a package for the design of electric machines and drives." Accessed May 2023.

[63] K. Lau, G. Goodwin, and R. M'Closkey, "Properties of modulated and demodulated systems with implications to feedback limitations," *Automatica*, vol. 41, pp. 2123–2129, dec 2005.